Author's Response

Dear Editor and Reviewers,

we provide below the responses to each issue raised by the reviewers and we attach also the manuscript file with all the changes tracked. We would like to thank all the constructive comments and questions pointed out by the reviewers, to which we tried to answer in the most correct and thorough way possible.

In the following lines we repeat the referee's statements with our replies to them reported in bold font, while the manuscript changes are highlighted in blue-colored text.

Best regards,
Letizia Anderlini (on behalf of co-authors)

Reviewer #1 Anonymous

Response to "Review of SE-manuscript Anderlini et al. 2020"

We are grateful for the constructive comments provided by the anonymous referee. He/she raises two main concerns, i.e. the seismic catalogs used and the fault geometry definition, which are addressed in detail below. Furthermore, specific comments to individual points of the manuscript are provided. In the following, we will repeat the referee's statements and our reply to it (in bold font).

The study regards a topic of importance and interest and the manuscript in general is well structured and well written. The study area along the southern boundary of the Italian Eastern Southern Alps (ESA) is known for a high seismic hazard in combination with a low-to-moderate plate tectonic strain that is difficult to locally pinpoint to specific faults. The paper reviews the various publications that recently documented different parts of the geodetically determined (mainly horizontal) strain and the seismic deformation rates that exhibit significant discrepancies across the ESA thrust fault system. As the title of the manuscript implies, new insight is gained by combining the existing tectonic, seismic and geodetic information with additional vertical geodetic velocity data integrated from GPS, InSAR and leveling measurements.

I congratulate the authors to a good study and manuscript. I do have only a few general points for consideration by the authors and a number of smaller issues with some of the figures that I list below. Overall, I believe the entity of these issues would require just MODERATE REVISION.

In the first of their main chapters –chapter 3 Geodetic Observations- the authors provide not only a careful evaluation and combination of InSAR and GPS observations but also a discussion of the different geodetic measurement techniques and their resulting data. This certainly denotes a very useful commented summary review of geodetic techniques also for the non-specialist readership. In the subsequent second main chapter of the paper, the

authors develop a 2D fault model to represent the ESA front fault system and to interpret the horizontal and vertical strain gradients measured across the fault system. Again the modelling is characterized by careful evaluation and balanced weighting of the different geodetic data. While the model seems to generally „reproduce the observed velocity gradients from all (geodetic) data sets“, „geological and geomorphological data appears not to be fully consistent“ and I would also list the seismologic information as not being fully consistent. I fully agree with the conclusions by the authors, but I do believe that in correspondence with the careful evaluation and interpretations of the fit and the discrepancies (1) between different geodetic data sets and (2) between the best-fit 2D fault model and the geodetic data, an additional conclusion would not only be appropriate but necessary: we need better seismicity and better geological subsurface structure information. The former obviously does not understandably correspond with the geodetic data assembly and the latter is very poorly constrained or entirely speculative (see also comment below).

We agree with the reviewer, additional new geological (surface and subsurface) and seismological data are certainly required to better interpret the geodetic signal and we add this sentence:
“However, important constraints from new seismicity data and new surface and subsurface geological observations will be required, together with denser GNSS data, to better constrain the tectonic rates and seismogenic potential in this area.”

The seismicity shown in Figures 1 and 3 suffers from several questions regarding the consistency. (1) the time periods are not the same but do overlap between 2012 and 2017. Are you showing events from both data sets for this overlap time? (2) How to the events of the two data sets compare during this overlap time?

We thank the reviewer for this comment that gives us the opportunity to fix an issue that can generate confusion in the readers. We agree that the use of two seismic catalogues, with spatial and temporal overlaps is misleading. We intended to use the two catalogues for illustration purposes, but we acknowledge that this is causing confusion.
Yes, there is overlap between the two catalogues, and the events present in both catalogues (for the overlapping period, 2012-2017) are plotted twice, in slightly different locations (and different colors). The intent of the figure was to acknowledge the presence of this high-resolution seismic catalogue, presented in a recent work (Romano et al., 2019) that has been used to provide a “Portrait of the Montello Thrust”. We do not aim at any quantitative comparisons between seismic and geodetic strain rates. We have modified figures 1 and 3, plotting only the OGS bulletin data in Fig. 1, to give a regional overview of the spatial distribution of instrumental seismicity from 2000, and the high-resolution catalogue from Romano et al. (2019), in the 2012-2017 time-interval, in Fig. 3, for comparison with subsurface structures, focal mechanisms and model geometry.

(3) How comes much fewer events yellow-red are seen within broken line box in Fig. 1 than visible in cross section in Fig. 3? (4) Where does the obvious cluster seen in Fig. 3 at 10km depth between 45km and 65km profile distance locate in Fig1 map view?

The seismicity overlaps in Fig. 1 and in Fig. 3, but the symbols (scaled with magnitude) in Fig. 1 are much smaller than in Fig. 3. The two figures are now re-drawn considering this comment and the previous one.

(5) Why do you project the seismicity across a band 50km wide onto a profile where you project the geodetic data only across a band 20km wide?

The GPS velocities are projected along a 35 km wide profile (see Section 4), not 20, and the same is done for seismicity, for which we plotted the earthquakes in the same swath profile. We have re-drawn this figure considering only Romano et al. (2019) earthquakes. The dashed boxes in Fig. 2 and Fig. 3 are the same, and used to project GPS velocities and plot instrumental seismicity. We removed the dashed box in Fig. 1 that could generate confusion.

How do the fault plane solutions compare with each other, with the geologic fault geometries (Fig. 3) and with your final model (Fig. 7)?

In general we see some correlation between thrust faulting mechanisms and geological structures. The focal mechanisms plotted in this figure come from two local and temporary experiments (Anselmi et al. 2011 and Danesi et al. 2015). We acknowledge, and better state in the Discussion section of the manuscript, that the hypocentral depths suffer for the use of different seismic velocity models. In particular, low-dipping thrust events on the Montello flat (from Danesi et al., 2015) are considered reliable, and used to constraint the depth of the decollement in the dislocation model.

In Figure 3 you show the subsurface geometries of the ESA frontal fault system and as reference you refer in Figure caption and in text (lines 255 and 267) to Castellarin et al. 2006 („The gray continuous and dashed lines represent major and secondary faults digitized from the TRANSALP profile interpretation (modified from Castellarin et al., 2006). MT = Montello thrust, MBT = Montello backthrust, BV = Bassano–Valdobbiadene thrust, BL = Belluno thrust, VS = Valsugana thrust. “). In Castellarin et al. 2006 Fig. 7 is showing a geologic interpretation of vibroseismic image (down to 5km) and in Fig.8 a geologic interpretation of seismic time section again down to 5km and these figures document a profile that runs across the Montello Hill within the study region of this paper. These high-resolution seismic images and their geologic interpretations significantly differ in even the most prominent geometries with the interpretation shown in Fig. 3 of this study.

In figure 7 and 8 of Castellarin et al., 2006 the vertical scale is in seconds (5 s) probably TWT but it is not specified, therefore we suppose the sections presented are not depth migrated. In this case it is difficult to retrieve from these figures the exact geometry of the drawn fault lines, since the rocks involved are quite different from metamorphic to carbonatic and sandstone units characterized by a large variability in seismic waves velocities (ca 3-8 km/s). Differently, Figure 11 of Castellarin et al., 2006 presents a simplified general interpretation of the TRANSALP profile (TRANSALP Working Group, 2002), it is depth migrated, and thus it provides a real interpreted geometry for the tectonic structures presented even if with less details.

Rather, in Castellarin et al. 2006 Fig. 11 (see included figure below) entitled „simplified general interpretation of the TRANSALP profile there is shown a major detachment fault system separating and translating the imbricated upper crust at about 10km-12km depth from the middle and lower continental crust of Adria. It is the geometry of these fault

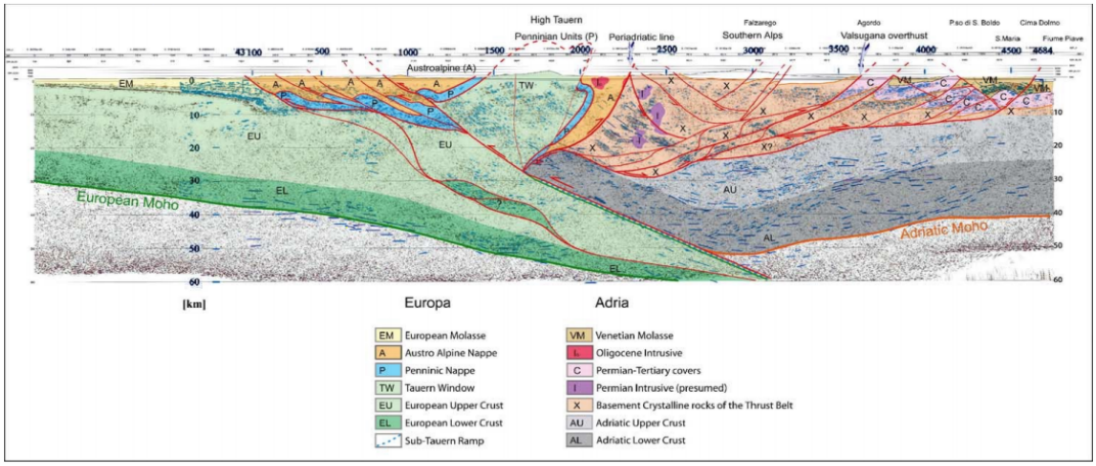

Fig. 11 Castellarin et al. 2006

system shown in red solid lines that seems to have been used for the model shown in Figure 3 of the current study. It seems difficult though to correlate the reflectivity image in fig.11 with the presented fault interpretation since (1) the reflectivity ends at 8km depth, (2) the shallow parts of the fault cut across well-documented continuous seismic signals and (3) no seismic evidence is visible for the detachment fault system at 10km to 12km depth. It is difficult to understand why the local high-resolution images and geologic interpretation would be ignored and a „simplified general interpretation“ of regional scale would be used for a local study like the current one. You must provide details of what and why you „modified from Castellarin et al. 2006“ and you must refer to the precise Figure that you used from Castellarin et al. 2006 and provide reasons for your specific choice.

As the reviewer rightly intuited, we used Figure 11 of Castellarin et al. 2006 for the fault geometries proposed in Figure 3. We are aware of the limits of its interpretation, but the profile is appropriate for the purposes of the modeling approach. Indeed in the context of the interseismic deformation modeling, the shallow portion of the faults, that are supposed to be locked, are not responsible of the observed deformation that is conversely due to the deep aseismically creeping fault portions (e.g. Vergne et al., 2001; Daout et al., 2006). For this reason our model is not influenced by the specific geometries of shallow fault structures, but on the contrary by the deep detachment fault system that aseismically slips. Moreover the used geometric interpretation is in agreement with the recorded seismicity and the available focal mechanisms (Figure 3) providing important constraints on the fault decollement. For completeness we provide below the comparison of the geometric sketch shown on Figure 6 of the manuscript with the part of Figure 11 of Castellarin et al. (2006), that we used to set up the fault geometry. We are aware that seismic interpretation have wide margins of error but the constraints provided by the instrumental seismicity reinforce the chosen model.

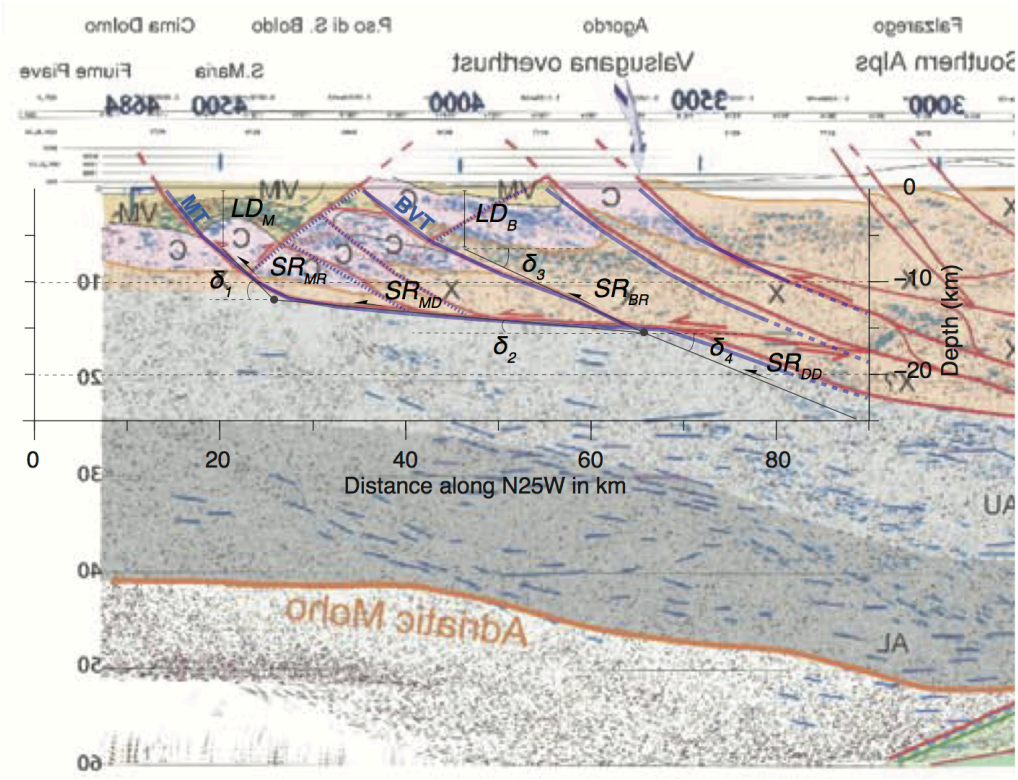

Here we compare the same sketch (Figure 6) with the local high-resolution geological interpretation provided by Galadini et al. (2005) in Figure 11, proving that the proposed geometry is also compatible with this surficial geological cross section.

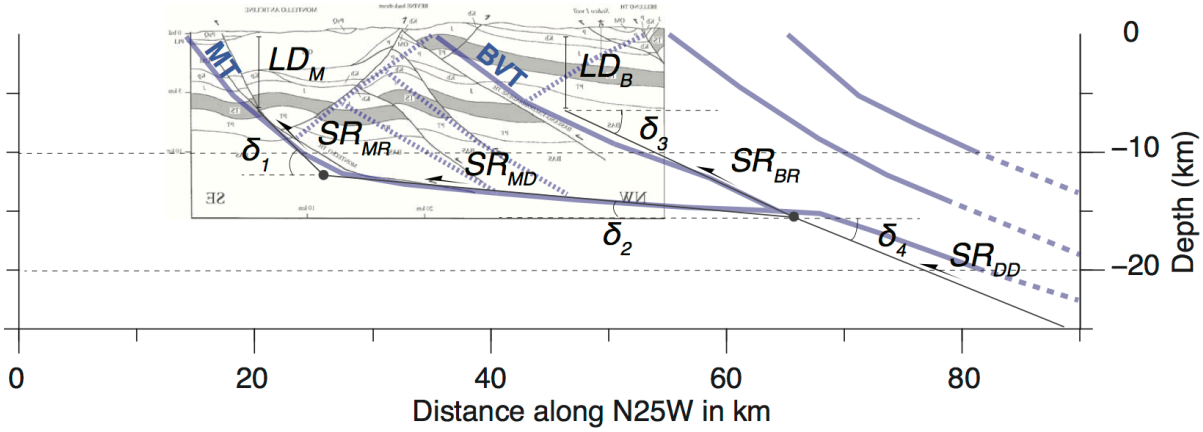

Finally, it seems the major change you imposed regards the introduction of the SRDD (Figs. 6 and 7) that seems to play a major role in your model. However, please consider that the introduction of this and the stipulated other parallel faults dipping down to 20km are purly speculative as no evidence in the TRANSALP seismic data can be found in Castellarin et al. 2006 and in addition such fault contradict the concept and model documented in Fig. 11 with a pronounced and important subhorizontal detachment fault at 10-12km depth reaching far to the North beneath ESA.

As we show in the sketch above, the proposed fault geometry is in overall agreement with the interpretation documented in Fig. 11 of Castellarin et al. (2006), where the considered deep detachment faults follow the geometry indicated by the profile. The

Deep Decollement (DD) is derived by the interpretation of TRANSALP profile that highlights at ~15 km depth a possible deepening of the basement rocks, that is however at the border of our model, where we have few data, playing a marginal role in the fault system. Anyway we agree that faults dipping down to 20km from the TRANSALP interpretation are speculative and that these structures might be affected by wide uncertainties.

Specific comments:

Figure 1. Much to busy figure. Reduce opacity of topography grey. Sizes of circles blue-purple and yellow-red reflect magnitude, please show scale. Rotation of Adria relative to Europe – what exactly is used as stable Europe relative point? What portion of Adria is rotating – your inset suggests all of Adria but this is difficult to justify for westernmost Adria. Explain why two different periods 2000-2017 and 2012-2018 are combined and what does this mean for the seismicity to be representative for?

As stated above, we fix the issue removing from this figure the seismicity from Romano et al. (2019), yellow-red symbols, that covers the 2012-2017 period. We followed all the graphical suggestions. As regard the Adria-Eurasia relative rotation, we add in the inset the position of the GPS stations used to determine the Adria rotation pole in Serpelloni et al., (2016), where as well are reported all the site used to represent the stable Eurasian plate.

Figure 2. increase size of colored circles. If Adria is rotating relative to Europe as shown in Fig. 1, what would be the local motions of the stations within ESA relative to the rotating Adria look like?

Ok, we modified the figure accordingly to the comment. The figure already shows the horizontal velocities of GPS stations with respect to the Adria plate. Indeed the GPS stations located in the Venetian, Friuli and Emilian Po Plains (see Figure 1 for geographical references) show almost zero horizontal velocities being representative of a stable plate (in this specific reference frame, of course).

Figure 3. red dots and their uncertainty estimates: since profile runs oblique to rotation minor circles of Adria, do these uncertainty estimates include the relative differences of rotating Adria?

Yes, the uncertainties are projected along the profile direction.

Note that the seismicity shown along the profile AB extends beyond the dashed box shown in Fig.2, box in Fig. 2 should be as long as AB profile in Fig. 1 and 3. What are the hypocenter location uncertainties?

The box in Fig. 1 was shown only for indicating the study area, but we have now removed from the figure to avoid confusion. In Figure 3 we now plot only the high-resolution earthquake catalogue from Romano et al. (2019), in the 2012-2017 time-interval, selecting all the events for which hypocentral uncertainties are provided, which are of the order of 1-2 km. In particular more than 90% of the events have the

horizontal and vertical errors (ERH and ERZ) less than 1.5 km and 3 km, respectively, and the whole dataset has a mean value of ERH = 0.7 km and of ERZ = 1.1 km.

Are the hypocenter parameters of the two earthquake data sets calculated with the same velocity model, with the same magnitude?

No, the velocity models are different, and since the one used by Romano et al. (2019) is more appropriate for the study region, we decide now to show in this figure only these earthquakes, and not those ones from the OGS bulletin.

Please add hypocenter depth color codes as in Fig. 1. Regarding geometry of proposed fault system see critical comment above.

Ok, done.

Figure4. „(after the ramp removal)“ please explain or refer to text. bottom panels please refer to red dots in figure caption.

Ok, done

Figure 6. Regarding geometry of subsurface model see critical comment above.

For the proposed geometry see the answer reported for the comment above.

References

Anselmi, M., Govoni, A., De Gori, P., and Chiarabba, C.: Seismicity and velocity structures along the south-Alpine thrust front of the Venetian Alps (NE-Italy), Tectonophysics 513, 37–48, doi:10.1016/j.tecto.2011.09.023, 2011.

Castellarin, A., Vai, G.B., and Cantelli, L.: The Alpine evolution of the Southern Alps around the Giudicarie faults: A Late Cretaceous to Early Eocene transfer zone, Tectonophysics, 414, 203–223, doi:10.1016/j.tecto.2005.10.019, 2006.

Danesi, S., Pondrelli, S., Salimbeni, S., Cavaliere, A., Serpelloni, E., Danecek, P., Lovati, S., and Massa, M.: Active deformation and seismicity in the Southern Alps (Italy): The Montello hill as a case study, Tectonophysics 653, 95–108, doi:10.1016/j.tecto.2015.03.028, 2015.

Daout, S., Barbot, S., Peltzer, G., Doin, M.P., Liu, Z., and Jolivet, R.: Constraining the kinematics of metropolitan Los Angeles faults with a slip-partitioning model, Geophys. Res. Lett., 43, 11192–11201, doi:10.1002/2016GL071061, 2016.

Galadini, F., Poli, M.E., and Zanferrari, A.: Seismogenic sources potentially responsible for earthquakes with M≥ 6 in the eastern Southern Alps (Thiene-Udine sector, NE Italy), Geophys. J. Int., 161, 739–762. doi:10.1111/j.1365-246x.2005.02571.x, 2005.

Romano, M.A., Peruzza, L., Garbin, M., Priolo, E., and Picotti, V.: Microseismic Portrait of the Montello Thrust (Southeastern Alps, Italy) from a Dense High-Quality Seismic Network, Seismol. Res. Lett., 1–16. doi:10.1785/0220180387, 2019.

TRANSALP Working Group: First deep seismic reflection images of the Eastern Alps reveal giant crustal wedges and transcrustal ramps. Geophys. Res. Lett. 29, 10. doi:10.1029/ 2002GL014911, 2002.

Vergne, J., Cattin, R., and Avouac, J.P.: On the use of dislocations to model interseismic strain and stress build-up at intracontinental thrust faults, Geophysical Journal International, 147, 155–162, 2001.

Reviewer #2 Romain Jolivet

Response to review of Romain Jolivet (Referee)

We are grateful for the constructive feedbacks provided by Romain Jolivet. He raises three main issues, which are addressed in detail below, answering as thoroughly as possible at each point raised. Furthermore, specific comments to individual cases of the manuscript are provided. In the following, we will repeat the referee's statements and our reply to it (in bold font).

In this article, Anderlini et al propose to apply an approach that has been applied extensively to various tectonically active regions globally but, to my knowledge, not very often to the actively deforming areas in the alps. The authors first derive some velocity fields from GNSS and InSAR data and describe some available leveling measurements. They propose a decomposition of the InSAR velocity maps into vertical and horizontal velocity fields, which are then discussed. They move on to a very classic 2D elastic modeling of the deformation to explore potential stress accumulation when considering the active faults in the region.
In general, the paper is well written and I do not see major issues with it. However, some points need to be discussed and my comments might require a bit of work. Figures are clear (although texts could be emphasized on the maps). I see three main issues in the paper that require being fixed before publication but, after that is done, this paper will be a very interesting contribution to the discussion on how active are these frontal thrusts surrounding the Alps. I hence recommend moderate revisions and I am looking forward to see a revised version of the article. I have set major revisions in the review system because there is no intermediate step between minor and major for this journal.

Main Comments:
1 - There is very little discussion on how the selection of the data is performed to avoid the effect of subsidence in the plain. The authors propose a strict threshold of -0.5 mm/yr of vertical motion below which any deformation is considered as subsidence and removed from the data fed into the model. In my opinion, this is risky, as some long wavelength subsidence might affect the general pattern of deformation. If subsidence is high near the coast and in the plain, as implied by the data, then there should be a bending effect that will affect the whole dataset. The wavelength of such bending might depend on the processes at stake, but it is unlikely that a strict threshold will allow to bypass this discussion.

We understand the raised point. We are aware that in this region several different deformation sources are involved besides tectonic loading. Concerning the widespread subsidence in the Venetian plain, there is an extensive literature discussing all the processes involved but no bending effects are mentioned. To justify the chosen threshold, we add in Section 3.4 an in-depth description of the ongoing processes as follows: "Several studies investigated subsidence processes in the Venetian plain (e.g. Carminati and Di Donato, 1999; Carbognin et al., 2004; Teatini et al., 2005; Bock et al., 2012), which is due to three main causes (both of natural and anthropogenic non-tectonic origin): 1- aquifer compaction after the strong groundwater withdrawal in the second half of the last century (e.g. Gatto and Carbognin, 1981; Carbognin et al., 1995); 2- uncontrolled expansion of coastal settlements and industrial activities (e.g. Tosi et al., 2002); 3- recent sediment compaction (e.g. Brambati et al., 2003; Fontana et al., 2008). As we can see from the profile A-B of Fig.5, subsidence rates increase from the center of the plain towards the coasts as due to the sum of the aforementioned processes." Since none of the these processes can be taken into account in our model, we choose the threshold of -0.5 mm/year and we add in the manuscript a reference to Section 3.4 to justify the choice.

My point mainly arises from the fact that (and this is an issue) your model does not really fit the InSAR and leveling data you are using. The relatively high rates of uplift measured in the north are not correctly predicted by your model (which underdetermines uplift) while the low rates to the south are over-determined. It seems that there is a constant trend between the geodetic data and the model. Geodetic data agree well with each other, which is great, but the model does not really manage to catch up. This could also be caused by isostatic adjustment adding a long wavelength deformation (i.e. a wavelength longer than profile you have established). One possibility would be to explore the effect of a linear trend (or whatever long-wavelength pattern you can think of) that would represent the long wavelength deformation needed on top of what results from dislocations in an elastic half space. This requires exploring the tradeoff between this long wavelength deformation signal and what is predicted in terms of locking depth and slip rates for both faults. It should have an impact and should be accounted for in the inverse problem.

As concern the uplift of the Alps, the processes responsible for this signal are: 1) active tectonic shortening, which is expected to be significant in the Eastern Southern Alps due to the active compressional Adria-Eurasia convergence 2) glacial isostatic adjustment (GIA), which is expected to be higher in the center of the Alpine chain 3) erosional unloading 4) geodynamic processes due to mantle flows. We refer to Sternai et al. (2019) for a review of the aforementioned processes. Considering that for the eastern Alps the contribution to the uplift rates due to mantle flows (process n. 4) seems to be uncertain and negligible (Sternai et al., 2019), plausible estimates of the isostatic adjustment to deglaciation (n. 2) and erosion (n. 3) may account for up to ~80% of the budget of observed uplift rates in the Eastern Alps (see Fig.8 of Sternai et al., 2019).

Several models have been proposed to quantify the Alpine uplift due to the glacio-isostatic contribution (e.g. Barletta et al., 2006; Spada et al. 2009; Norton and Hampel, 2010; Mey et al., 2016) and the erosional unloading (e.g. Sternai et al., 2012, 2019; Mey et al., 2016), mostly by means of large scale models with a poor spatial resolution. However, it is known that these models are less reliable at the border of the Alpine ice cap (Sternai et al., 2019), where our study area is located. In the original manuscript we

widely discussed about this issue in Section 6 (L380-391), and given these uncertainties, we have not considered to correct the geodetic observations for a long-wavelength isostatic contribute. However we acknowledged its importance, stating that "a possible correction for these contributions would slightly reduce the intensity of uplift rates. If it were possible to apply such a correction, the slip-rates estimates on the fault planes could be slightly reduced, in turn decreasing a little the seismogenic potential associated with the MT and BVT faults." (L389-391).

In order to provide a quantitative estimate, we made a test by inverting for slip-rates and locking-depths assuming the same fault geometry, but geodetic rates corrected for a long-wavelength vertical signal, which is here assumed as a linear gradient of uplift rate along 100 km of distance. Considering the mean uplift rate of 1 mm/year in the northernmost sector of the study area (the Dolomites), we choose 0.8 mm/year (80%) as maximum vertical isostatic adjustment to be removed from the observed vertical velocities. In particular we consider a linear trend (with a slope of 0.008 mm/(year*km)) that starts from Treviso city (TREV and TVSO GPS stations), along the same direction of the profile indicated in Fig. 2, and reaching the limit of 0.8 mm/year of uplift rate in correspondence of POZZ station.

We are aware that this model is purely speculative and based on strong assumptions, but we can consider this simple approach as an upper-bound case on how considering or not these long-wavelength signal may affect the results of the inversion.

We remove this linear signal from all the geodetic datasets, i.e. from the vertical component of GPS velocities, leveling data and subsampled InSAR LoS rates, and perform the inversion of the modified velocities in order to estimate locking depths and slip rates for the proposed fault geometry. Due to these changes in the input observations, we re-evaluate the relative weighting factor *Wsar*, finding an optimal value of 0.68.

The results of the inversion are presented in the Figure A1 (below), showing the same information reported in Figure 7 of the manuscript with a few differences: the purple line in the section of the vertical rates represents the linear gradient we removed, and light gray dots indicate the unmodified original datasets, while all the other data are corrected for the linear gradient. In the bottom panel the estimated parameters (locking depth and dip-slip rates) are reported, as well as in the following table.

Dataset	LD Montello Ramp	LD Bassano Ramp	Slip rate Montello Ramp	Slip rate Montello Flat	Slip rate Bassano Ramp	Slip rate Deep Ramp	RMSE GPS	RMSE LEV	RMSE InSAR
Corrected data	4.6 km	8.6 km	0.5 mm/a	0.35 mm/a	2.0 mm/a	2.3 mm/a	0.46 mm/a	0.57 mm/a	0.59 mm/a
Original Data	$5.6_{-3.8}^{+3.5}$ km	$9.1_{-0.6}^{+1.3}$ km	$0.5_{-0.1}^{+0.2}$ mm/a	0.4 ± 0.1 mm/a	$2.1_{-0.6}^{+0.8}$ mm/a	$2.5_{-0.7}^{+0.8}$ mm/a	0.44 mm/a	0.72 mm/a	0.66 mm/a

We observe that there are no substantial differences with respect to the optimal fault parameters obtained with the original dataset (Table 2 of manuscript, also reported above). This correction lead to a slight decrease of slip rates and locking depths, which are, however, all largely within the error bounds of the optimal model. We can note that at the expense of a slight increase of GPS RMSE, the misfit for the other data decreases,

allowing for a better balancing among the three dataset. The slight increase of GPS residuals is mainly due to the misfit between the model and the vertical velocities to the north (see PASS and FDOS in the figure below) that depends, however, on the vertical gradient we remove which is steeper than the gradients expected from large scale models. In light of these results we do not aim at correcting the geodetic velocities for an isostatic uplift signal, considering also that the estimated fault parameters doesn't provide significant differences in terms of slip-rates and locking depths. Most of these considerations have been added in Section 6 of the main text and the specific details in the Supplement.

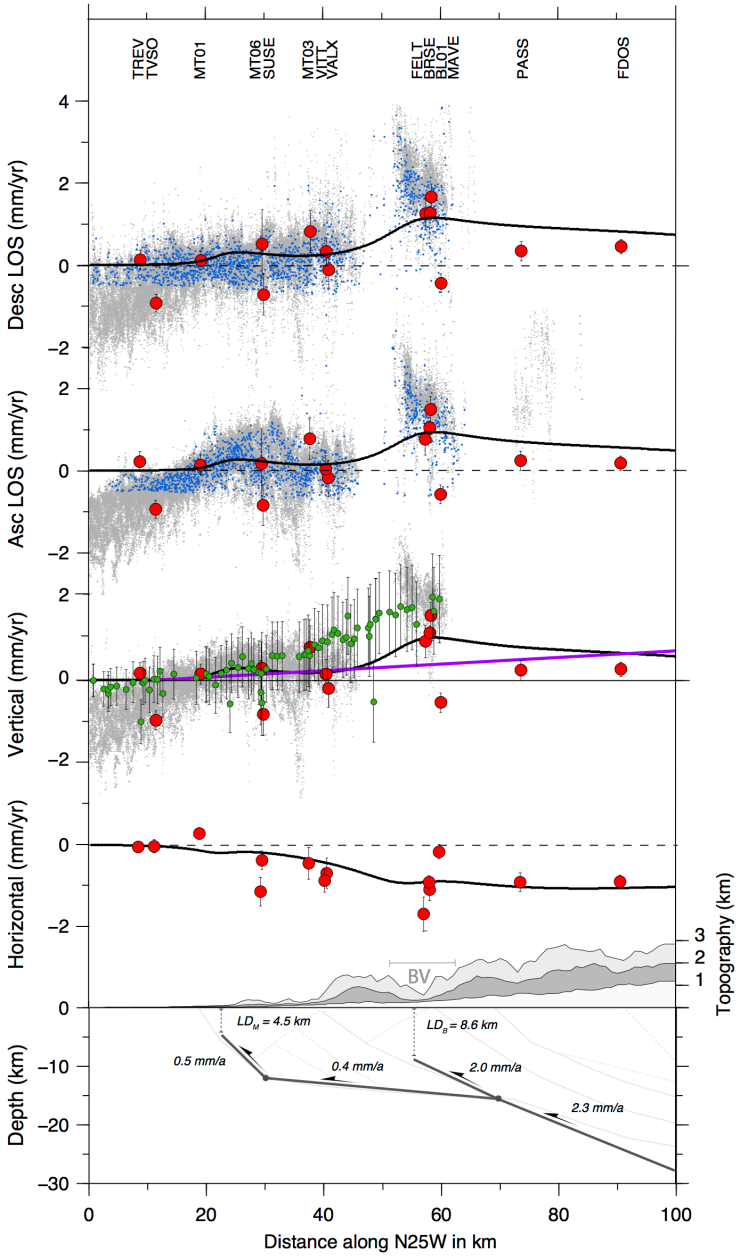

Figure A1: Cross sections, across the A-B profile of Fig. 2 of the manuscript, showing the modeled (black lines) horizontal and vertical velocities, as well as the SAR ascending and descending LoS rates, along with the measured ones. Green points indicate leveling data and small blue dots represent the subsampled InSAR LOS rates used during the inversion. The bottom panel reports the optimal fault geometry with dip-slip rates and locking depths estimates. BV: Belluno valley

2 - There is not enough details on how the InSAR data have been processed. Although the SBAS method is now quite known, quantitative information is required to assess the quality of the velocity field. It is not only because it correlates quite well with GPS that everything has been done right. For instance, correcting for tropospheric delays using a phase-topography correlation when trying to unravel a signal that correlates as well with topography is dangerous. One could easily mix deformation with tropospheric delays.

We used the SARScape module of ENVI software, provided by Harris Geospatial Solutions (http://sarmap.ch/tutorials/sbas_tutorial_V_2_0.pdf), to perform SBAS analysis. The SBAS algorithm includes several steps (e.g Pasquali et al. 2014): creation of a connection graph (computing all differential interferograms from the input image stack according to the chosen criteria for temporal and geometric baselines), differential interferogram generation (spectral shift and adaptive filtering), phase unwrapping, orbit refinement and re-flattening, first estimation of the average displacement, atmospheric phase screen removal, and final estimation of the average displacement and mean ground velocity. In our study, we achieved a ground resolution of 90 m by using a multi-looking factor of 4 in range and 20 in the azimuth. All the Single Look Complex images (SLC) are coregistered in the master image geometry using a 90-m Digital Elevation Model (DEM) provided by the Shuttle Radar Topography Mission (SRTM). The topographic phase contribution was removed using the DEM, too. We applied the Goldstein filter (Goldstein and Werner, 1998) to smooth the differential phase and use precise DORIS orbits (provided by the European Space Agency) and the SRTM DEM to correct the computed interferograms from possible orbital ramps. We used the Delauney minimum cost flow (MCF) network (Constantini, 1998) along with the Delaunay method to unwrap the differential interferograms. The unwrapping coherence threshold at this stage was set to 0.3. We selected approximately several tens Ground Control Points (GCP) mainly at the borders of the processed frame, to perform the refinement and re-flattening step. Subsequently, the average displacement rate and residual height-correction factors were estimated by inverting a linear system through the Singular Value Decomposition method. Then, low-pass and high-pass spatial filters were used for the time-series images, to screen and remove the atmospheric phase component. In fact, the starting idea is that atmosphere is correlated in space but not in time. We considered two moving windows of 365 days and 1200 meters for the two filters (High and low pass). Finally, the solution of the inversion was geocoded through the used DEM. All of the final displacement measurements were obtained onto the satellite line of sight (LOS) direction and geocoded in the UTM 33N reference system.

Furthermore, since the region has quite strong topographic gradients, unwrapping is probably challenging and there is not a word on that (which method is used for unwrapping? In general, which software is used to compute the interferograms?).

As mentioned above, we adopted the Minimum Cost Flow (MCF) algorithm with the Delauney triangulation method. The latter helps the propagation of the unwrapping solution to reach coherent pixels also if they are separated by non-coherent areas. In fact, as you can see from in Figure 4 of the main text, the solution was able to overcome only the first mountainous chain propagating through the valleys. This was exactly due the presence of quite strong topographic gradients, as the reviewer has noticed. All the

A-InSAR processing chain, as already mentioned above, was computed using the Sarscape software.

Would it be possible to see a baseline plot?

Yes, the following figure shows the obtained connections graph and baselines distribution for the ASAR-Envisat datasets of both ascending and descending orbits. We choose interferometric pairs with a perpendicular baseline smaller than 450 meters and a temporal baseline lower than 600 days for both the orbits. The figure is now added in the Supplement.

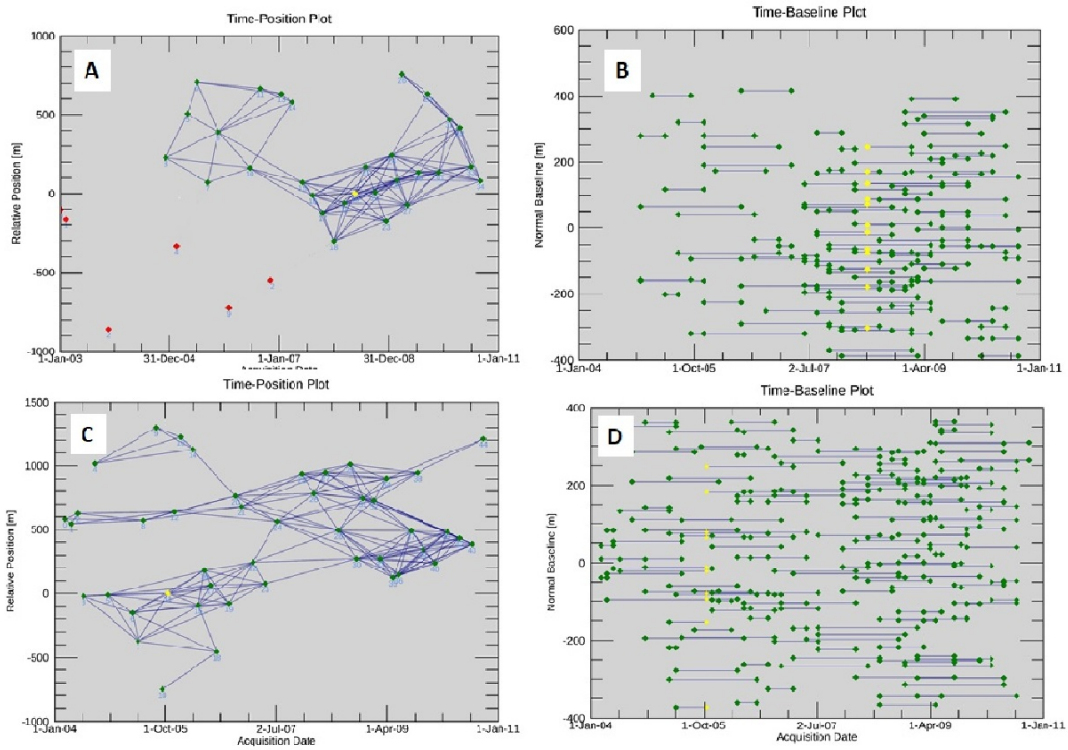

Fig. A2: (A) Considered pairs connection graph for the descending SAR orbit; (B) Considered baseline graph for the descending SAR orbit; (C) Considered connection graph for the ascending SAR orbit; (D) Considered baseline graph for the ascending SAR orbit.

Also, is there connectivity issues within the network, considering potential unwrapping issues?

Looking at Figure A2, we are confident that no remarkable unwrapping issues were found during such a step. Moreover, before following the inversion steps, we checked each interferogram discarding all the pairs showing clear unwrapping errors and keeping the ones with low atmospheric noise.

What is the RMS of the reconstruction of your time series?

We calculate the RMS considering one of the different possible formulas and exactly the following: $RMSError = \sqrt{1 - r^2} SD_y$ where *SDy* is the standard deviation of each retrieved displacement time series and *r* is the correlation coefficient between the time series and the considered acquisitions. RMS is a measure of the fitting quality

geocoded. It is the RMSE expressed in millimeters. The higher this value the worse the fitting and inversion quality. The RMS about all the time series retrieval is showed in the figure A3:

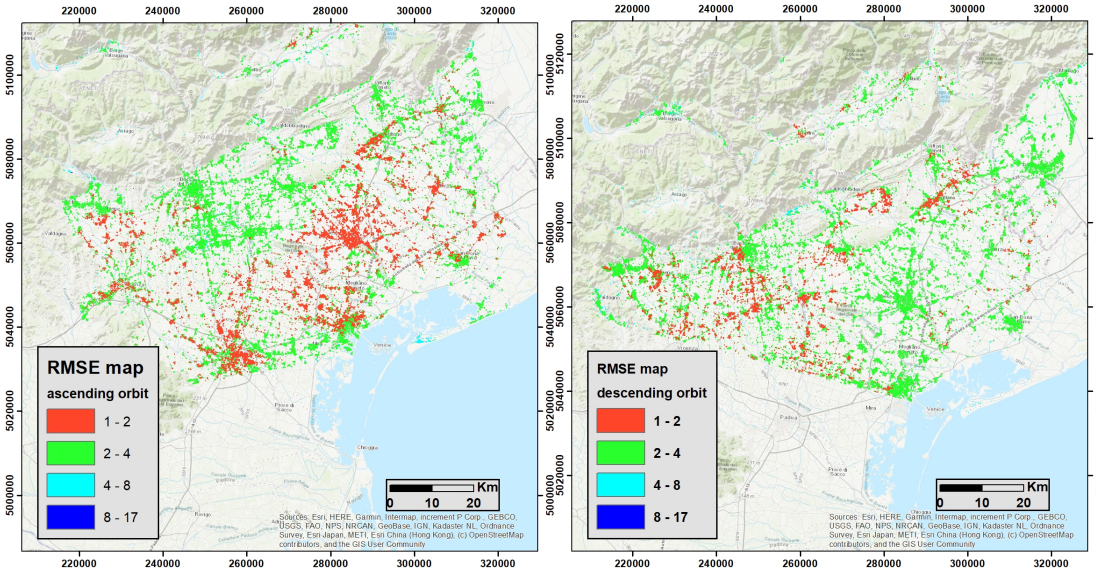

Fig. A3: RMSE maps of the displacement time series for the ascending and descending orbits

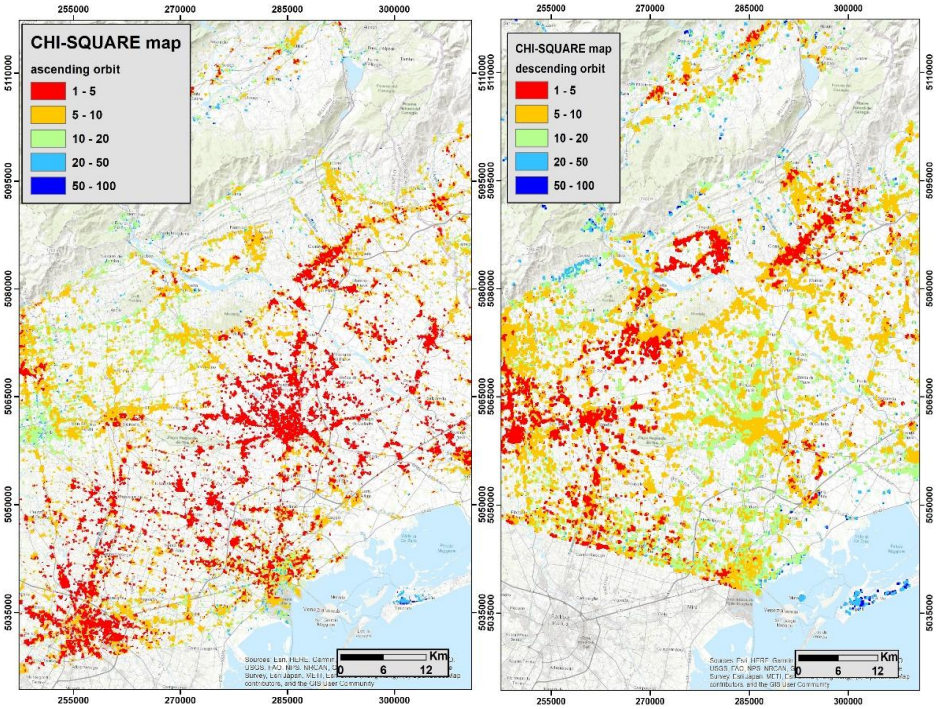

Fig. A4: Chi-Square values for the ascending and descending orbits

How linear is the time series?

Initially, we considered a linear model in the inversion step then, in a second unwrapping run, the non-linearity is estimated from the residuals obtained as difference from the unwrapped phase and the linear model. One of the estimated parameters at the end of the processing chain is the Chi-square value (Figure A4) relative to each time series. Such a value is a non-dimensional number representing how much the time

series diverges from the linear behavior. Low values of the Chi-square indicates a quasi-linear trend of the displacement time series, high values for the contrary. In any case, the Chi-square test has to be considered carefully. In fact, high values do not mean not reliable result for that area. In fact the chi-square does not represent an absolute but relative parameter, in the meaning that it does not have a predefined maximum value (i.e. the interferometric coherence parameter) but can vary depending on the type of the movement present in the study area. So if there are zones with a non-linear behavior, such areas will show high chi-square values and vice-versa. In our case, high values of chi-square are greater than 100, thus values within 10-15% of the maximum can be considered representative of pixels having mostly linear behavior.

Is there a time dependent signal?

The retrieved patterns are mainly time independent, in the meaning that the most of the obtained ground deformation field shows a behavior tending towards the linear trend (red and orange areas in Figure A4)

There is much more details provided for the processing of GPS data and the processing of InSAR being much less standardized than GPS these days (especially with the old Envisat data) suggests there is a lot to be added in the manuscript.

We added much more info about the processing steps and the parameters setting adopted during the processing chain in the manuscript and in the Supplement.

Finally, a lot of people have developed comparable methods for InSAR downsampling and they deserve some credit (see Lohman & Simons 2005, Jolivet et al 2012, 2015 or Sudhaus & Jonsonn 2009 for instance, but there is many other papers mentioning this).

We agree with the reviewer, there is a lot of literature regarding downsampling methods of InSAR data. Indeed most of literature regarding downsampling methods of InSAR data analyzes coseismic and volcanic ground deformation. In these cases just a portion of the displacement map is characterized by high deformation gradient, thus the widely-used quadtree sampling method (e.g. Jónsson et al., 2002; Pedersen et al., 2003; Lohman and Simons, 2005; Metzger et al., 2011; Barnhart and Lohman, 2013) is appropriate. Indeed this algorithm reduce the number of data in order to represent the statistically significant portion of the signal (Jónsson et al., 2002) choosing a specific threshold value for the data variance in each iteration. This method has been applied also for interseismic studies (e.g. Jolivet et al., 2012; Maurer and Johnson, 2014; Xue et al., 2015) where, however, the signal-to-noise ratio of InSAR data is big enough to define an appropriate threshold value to avoid losing information of the deformation gradients. In our case, with low deformation gradients it is highly risky to apply a subsampling method that depends on the deformation signal itself. For this reason we apply an alternative method that uniformly reduce the density of pixels.

We add now a short description in Section 4 as follows: "Most of studies, performing a subsampling of InSAR data for geophysical inversions, use the quadtree sampling method (e.g. Jónsson et al., 2002; Pedersen et al., 2003; Lohman and Simons, 2005; Jolivet et al., 2012; Maurer and Johnson, 2014) that allows to reduce the number of data in order to represent the statistically significant portion of the displacement

signal (Jónsson et al., 2002). In our case, with low deformation gradients it is highly risky to apply a subsampling method that depends on the deformation signal itself. For this reason we apply an alternative method that uniformly reduce the density of pixels and the specific technical details are provided in the Supplement."

3 - The description of the inversion procedure is incomplete. The algorithm used to find the minimum of the cost function should be, at least, named.

We integrate the main text in Section 4 as follows: "The inversion method exploits a constrained, non-linear, derivative-based optimization algorithm (i.e. interior-point, see Byrd et al., 1999; Waltz et al., 2006). It allows to estimate the optimal parameter solution corresponding to a possible global minimum of the cost function representing the misfit between the model prediction and the geodetic measurements. These algorithms depend on the gradient and higher-order derivatives in order to guide them through misfit space, thus they can get trapped in a local minimum (Cervelli et al., 2001), providing the best results when the starting point is near the global minimum. However, in order to ensure that we find a global solution in the inversion, we tested several different initial guess founding always the same model estimate."

Furthermore, I suspect there is some regularization of the inverse problem involved (maybe not), but please mention it.

No, there is no regularization of the inverse problem, but we applied specific constraints to the parameter space to be investigated (such as locking depth within the elastic thickness and slip rates kinematically consistent among them). Indeed, we did not modify the relationship of the cost function (as it would be done in case of a regularization) that considers only the weighted misfit between observed and modeled velocities, but we took advantage of the specific options of the minimization algorithm described above, forcing the model to respect the imposed constraints.

In addition, the data covariance is not described. How is it determined? One cannot follow the deal with weights if one cannot reconstruct the covariance matrix.

We add in the manuscript in Section 4 the description of the data covariance: "The data covariance matrix is computed as follows: $cov = \Sigma R \Sigma^T$ **where** Σ **is the diagonal matrix of data uncertainty and *R* is the data correlation matrix, that is dimensionless, equal to one along the diagonal and the off-diagonal elements representing the correlation between each couple of data. Assuming the three geodetic dataset (GPS, InSAR and leveling) independent among them, the whole covariance matrix is composed by three independent blocks, one for each dataset. The correlation values are nonzero only for the three components of each GPS site, considering the measurements obtained by the GPS stations to be uncorrelated among them, and for the leveling data, following the approach of Árnadóttir et al. (1992). The InSAR data covariance matrix is instead diagonal with equal variance of 1 mm^2/year^2 for all the pixels."**

Then, there is a problem in the a posteriori covariance discussion. The authors mention the a posteriori covariance is derived for the linear terms while bootstrap is used for the non-linear

terms. In my opinion, the covariance that is derived here is obtained considering the least squares criterion (without regularization? with regularization? Is it just GˆT Cdˆ{-1} G ?) but then, it only corresponds to a “slice” of the model space, that slice corresponding to the best non-linear parameters obtained. If so, the a posteriori covariance is greatly underestimated as it is only representative of a joint marginal of the full a posteriori PDF.

We estimated the a-posteriori covariance matrix considering the least squares criterion (without regularization), but we agree with the reviewer that this is a partial representation of the slip rate uncertainties. We consider now to use the bootstrap distributions both for the linear and non-linear model terms providing the errors at 95% confidence bounds. Please see the answer below and the further specific details of the adopted approach. The error bounds for the estimated parameters have been corrected in Table 2 and in Figure 7 of the manuscript. For a full description of the model parameters uncertainties we provide also the trade-off distributions between parameters pairs, replacing Figure S6 of the supplementary material with the Figure A5 shown below. We can observe from these distributions that the locking depth estimates do not show any correlation with the other parameters, while for the dip-slip rates the strict correlation among them is representative of the kinematic conservation constraint, for which the only parameter we can consider independent is the deep decollement slip rate (underlined label of Figure A5). We have modified accordingly the main text, discussing in Section 5 the results in terms of fault parameters error bounds from the frequency histograms and of possible correlation between parameters from the trade-off scatter plots.

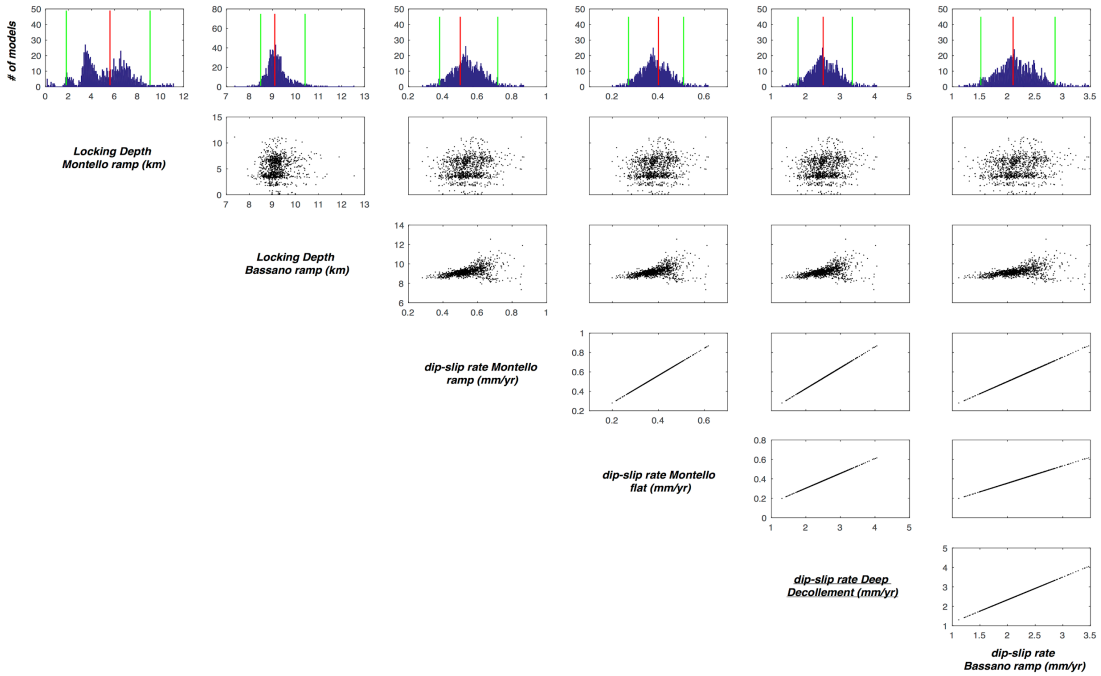

Fig A5: Model parameters distribution, obtained from the inversion of 1000 bootstrap re-samples of the original data (see Section 5). Top row: frequency histograms of the optimal fault parameters with the best optimal model (red line) and boundary values of 95 percentile confidence interval (green lines); see Table 2 for specific values. Other rows: scatter plots showing trade-off between parameter pairs.

Finally, one can see in supplementary material figure S6 that the range of possible models for the locking on the Montello Ramp is bi-modal.

Figure S6 (now, top row of Figure A5) doesn't show the range of possible models, but the collection of the optimal models we obtain randomly resampling the data by means of a bootstrap procedure used to estimate confidence intervals of the derived parameters (Segall and Davis, 1997) without making assumptions about the underlying statistics of errors (Amoruso and Crescentini, 2008). This method reflects the limitation of the data set used (Cervelli et al., 2001), and the bi-modal behavior of the locking depth of the Montello Ramp should be interpreted as representative of the low capability of the data to constrain this parameter, for which indeed the deformation signal is close to the techniques limits and velocity measurements appears noisy. These considerations are now added to the manuscript in Section 5 to provide a more complete description of the error bounds definition.

Then, if it is not Gaussian, why choosing the mean model?

We didn't choose the mean model but the optimal model estimated by the inversion algorithm, described above, using the whole geodetic dataset.

It seems that some models could be more appropriate. Would it be possible to sample for all the possible models using a Monte Carlo approach, which would give all the tradeoffs between the various parameters (and potentially solve the issue raised in my first comment)?

The bootstrap resampling provides optimal model distribution and the tradeoffs between the various parameters as shown in Figure A5.

For the minor comments, please refer to the annotated pdf I have sent along with my review.

We corrected the minor comments annotated in the pdf.

Looking forward to read an improved manuscript, if I am required to do so. I also strongly encourage the authors to add their geodetic data (i.e. the GPS, InSAR and leveling rates presented in the paper) to an online repository so other scientists can have a go at the modeling, once this study is published.

Since the GPS and leveling rates are already available in the Supplement, only InSAR velocities are made available in an online repository.

Please also note the supplement to this comment:
https://www.solid-earth-discuss.net/se-2020-10/se-2020-10-RC2-supplement.pdf

References

Amoruso, A., Crescentini, L., 2008. Inversion of synthetic geodetic data for the 1997 Colfiorito events: clues on the effects of layering, assessment of model parameter PDFs, and model selection criteria. Ann. Geophys., 51, doi:10.4401/ag-3027.

Árnadóttir, T., Segall, P., and Matthews, M., 1992. Resolving the discrepancy between geodetic and seismic fault models for the 1989 Loma Prieta, California, earthquake, Bulletin of the Seismological Society of America, 82, 2248–2255.

Barletta, V. R., C. Ferrari, G. Diolaiuti, T. Carnielli, R. Sabadini, C. Smiraglia, 2006. Glacier shrinkage and modeled uplift of the Alps, Geophys. Res. Lett., 33, L14307, doi:10.1029/2006GL026490

Barnhart, W. D., R. B. Lohman, 2013. Vertical partitioning of strain during earthquake sequences in Iran: Phantom earthquakes and triggered aseismic creep, Geophys. Res. Lett., 40, 819–823, doi:10.1002/grl.50201.

Bock, Y., S. Wdowinski, A. Ferretti, F. Novali, A. Fumagalli, 2012. Recent subsidence of the Venice Lagoon from continuous GPS and interferometric synthetic aperture radar, Geochem. Geophys. Geosyst., 13, Q03023, doi:10.1029/2011GC003976.

Brambati, A., L. Carbognin, T. Quaia, P. Teatini, L. Tosi, 2003. The Lagoon of Venice: Geological Setting, Evolution and Land Subsidence, Episodes, 26, 264-268.

Byrd, R.H., Hribar, M. E., Nocedal, J. 1999, "An Interior Point Algorithm for Large-Scale Nonlinear Programming," SIAM Journal on Optimization, Vol 9, No. 4, pp. 877–900.

Carbognin L., L. Tosi, P. Teatini, 1995. Analysis of actual land subsidence in Venice and its hinterland (Italy). In: Barends J.F., et al. (1995, eds.) - Land Subsidence, 129-137, A. A. Balkema, Rotterdam

Carbognin, L., P. Teatini, L. Tosi, 2004. Eustacy and land subsidence in the Venice Lagoon at the beginning of the new millennium. J. Marine System, 51(1–4), 345– 353.

Carminati, E., G. Di Donato, 1999. Separating natural and anthropogenic vertical movements in fast subsiding areas: The Po plain (N. Italy) case, Geophys. Res. Lett., 26, 2291–2294, doi:10.1029/1999GL900518.

Costantini, M. 1998. A novel phase unwrapping method based on network programming. IEEE Trans. Geosci. Remote Sens., 36, 3, 813-821, DOI: 10.1109/36.673674

Fontana, A., Mozzi, P., Bondesan, A., 2008. Alluvial megafans in the Veneto-Friuli Plain: Evidence of aggrading and erosive phases during Late Pleistocene and Holocene. Quaternary International, 189(1), 71–90

Gatto, P., Carbognin, L., 1981. The Lagoon of Venice: Natural environmental trend and man-induced modification. Hydrological Science Bulletin, 26(4), 379– 391

Goldstein, R., Werner, C., 1998. Radar interferogram filtering for geophysical applications. Geophysical Research Letter, 25, 21, 4035-4038, DOI: 10.1029/1998GL900033.

Jolivet, R., C. Lasserre, M.-P. Doin, S. Guillaso, G. Peltzer, R. Dailu, J. Sun, Z.-K. Shen, and X. Xu, 2012. Shallow creep on the Haiyuan Fault (Gansu, China) revealed by SAR Interferometry, J. Geophys. Res., 117, B06401, doi:10.1029/2011JB008732

Jònsson, S., H. A. Zebker, P. Segall, F. Amelung, 2002. Fault slip distribution of the 1999 Mw7.1 Hector Mine, California, earthquake, estimated from satellite radar and GPS measurements, Bull. Seismol. Soc. Am., 92(4), 1377–1389, doi:10.1785/0120000922.

Lohman, R. B., M. Simons, 2005. Some thoughts on the use of InSAR data to constrain models of surface deformation: Noise structure and data downsampling, Geochem. Geophys. Geosyst., 6, doi:10.1029/2004GC000841

Maurer, J., K. Johnson, 2014. Fault coupling and potential for earthquakes on the creeping section of the central San Andreas Fault, J. Geophys. Res. Solid Earth, 119, doi:10.1002/2013JB010741.

Metzger, S., Jónsson, S., Geirsson, H., 2011. Locking depth and slip-rate of the Húsavík Flatey fault, North Iceland, derived from continuous GPS data 2006–2010. Geophysical Journal International, 187: 564-576. doi:10.1111/j.1365-246X.2011.05176.x

Mey, J., Scherler, D., Wickert, A.D., Egholm, D.L., Tesauro, M., Schildgen, T., Strecker, M.R., 2016. Glacial isostatic uplift of the European Alps. Nature Commun. https://doi.org/10.1038/ncomms13382.

Norton, K.P., Hampel, A., 2010. Postglacial rebound promotes glacial re-advances – a case study from the European Alps. Terra Nova 22 (4), 297–302.

Pasquali, P., Cantone, A., Riccardi, P., Defilippi, M., Ogushi, F., Gagliano, S., Tamura, M., 2014. Mapping of ground deformations with interferometric stacking techniques, Land Application of Radar Remote Sensing, Holecz, F., Pasquali, P., Milisavljevic, N., Closson, D., IntechOpen, DOI: 10.5772/58225. Available online

Pedersen, R., Jònsson, S., Àrnadòttir, T., Sigmundsson, F. Feigl, K.L., 2003. Fault slip distribution of two June 2000 Mw6.5 earthquakes in South Iceland estimated from joint inversion of InSAR and GPS measurements, Earth. planet. Sci. Lett., 213(3–4), 487–502. doi:10.1016/S0012-821X(03)00302-9.

Segall, P., Davis, J. L., 1997. GPS applications for geodynamics and earthquake studies, Annu. Rev. Earth Planet. Sci., 23, 201–336.

Spada, G., Stocchi, P., Colleoni, F., 2009. Glacio–isostatic adjustment in the po plain and in the northern adriatic region. Pure Appl. Geophys. 1303–1318. https://doi.org/10.1007/s00024-004-0498-9.

Sternai, P., Herman, F., Champagnac, J.-D., Fox, M., Salcher, B., Willett, S.D., 2012. Preglacial topography of the European Alps. Geology 40 (12), 1067–1070.

Sternai, P., Sue, C., Husson, L., Serpelloni, E., Becker, T.W., Willett, S.D., Faccenna, C., Di Giulio, A., Spada, G., Jolivet, L., Valla, P., 2019. Present-day uplift of the European Alps: evaluating mechanisms and models of their relative contributions. Earth-Sci. Rev., 190, 589-604. https://doi.org/10.1016/j.earscirev.2019.01.005

Tosi, L., Carbognin, L., Teatini, P., Strozzi, T., Wegmüller, U., 2002. Evidence of the present relative land stability of Venice, Italy, from land, sea, and space observations, Geophysical Research Letters, 29(12), 1562, doi:10.1029/2001GL013211.

Waltz, R. A. , J. L. Morales, J. Nocedal, and D. Orban, 2006. "An interior algorithm for nonlinear optimization that combines line search and trust region steps," Mathematical Programming, Vol 107, No. 3, pp. 391–408.

Xue, L., S. Schwartz, Z. Liu, L. Feng, 2015. Interseismic megathrust coupling beneath the Nicoya Peninsula, Costa Rica, from the joint inversion of InSAR and GPS data, J. Geophys. Res. Solid Earth, 120, 3707–3722, doi:10.1002/2014JB011844.

Reviewer #3 Giovanni Monegato

Response to: SHORT COMMENT - GIOVANNI MONEGATO

We are grateful for the useful comments provided by Giovanni Monegato. He raises some specific comments to which we answered point by point. In the following, we will repeat the Monegato's statements and our reply to it (in bold font).

Dear Authors of the manuscript "New insights into active tectonics and seismogenic potential of the Italian Southern Alps from vertical geodetic velocities". This article is interesting in providing new geodetic data about deformations in this important sector of the Southern Alps. My remarks are related to the general approach that, here and in many similar works, the chronology and Quaternary stratigraphy are used for deformation rates assessment without using updated information about the landscape and sedimentary evolution of the study area. This happens because no geomorphologists or Quaternary stratigraphers are normally involved in such kind of studies. However, because of the importance of the age assessment is a key for the conclusions of these works, a more careful attention has to be paid. In the present work, many chronological references sound obsolete for the innovative scope of the research.

I listed the specific concerns for this work as follow:

Line 48: the "last deglaciation" is meant after the Last Glacial Maximum I would include the time span (19-11 ka BP according to Clark et al., 2012), for the Alps see also Ivy-Ochs (2015).

We agree with this comment and the text has been changed accordingly, the timing for global estimation of the age of the last deglaciation is set in the time window 19-11 Ka BP following Clark a et al., 2012 and references therein.

Line 52: Spada et al. (2009) is referred to the "last deglaciation" but not to the "present deglaciation" that refers to the ice waning after the Little Ice Age.

Thanks, we removed the reference from the text.

Lines 345-350: the use of old and updated terminology (Mindel-Riss-Würm) from old literature shows how the authors have not updated their knowledge about the Pleistocene stratigraphy of the study area. This was update in a review article by Carton et al. (2009), who provided a long list of radiocarbon data for the Piave catchment.

Even if the terminology is a bit old, a possible update would not provide further information on the considerations derived in this part of the manuscript.

Lines 353-354: the LGM is not at 20-18 ka but at 26-21 ka. I suggest to use Clark et al. (2009) for a global LGM or Monegato et al. (2017) for the Alpine LGM or Rossato et al. (2018) that gave the most updated chronology for the Veneto Prealps and piedmont plain. Also Pellegrini et al. (2005) included a useful chronology for the Belluno and Cesen-Col Visentin sector.

We agree with this comment and the text has been changed accordingly, the timing for LGM at global scale in terms of global ice-sheet and mountain-glacier extent is now set at 26-19 Ka BP following Clark et al., 2009, while the regional alpine LGM is set at 25-23 Ka BP with a second large advance of the ice at 23-21 Ka BP, following Monegato et al. (2017) and reference therein.

Line 366: maybe the Geological and geomorphological data appears thus not fully consistent just because the Authors need to use the proper updated dataset.

We have used all the available datasets of our knowledge.

Lines 368-369: Benedetti et al. (2000) rates for the Montello are affected by the wrong age estimation of the Montebelluna megafan, whose age was already given as pre-LGM by Fontana et al. (2008, 2014). I suggest to use these references for this discussion.

We agree with this comment and the text has been modified taking into account that the Montebelluna megafan can tentatively be considered older than 30,000 BP, thus of pre-LGM age, but probably still within the Upper Pleistocene (125 Ka BP), following Mozzi, 2005 and Fontana et al., 2014.

Lines 394-395: Benedetti et al. (2000) cannot be used for assessing the thickness of the Piave glacier in Belluno, because the work is not about Pleistocene glaciations. Pellegrini et al. (2005) and Carton et al. (2009) have to be considered instead. The Piave glacier was not an ice-sheet, which has to be used for the Alps (i.e., Alpine Ice Sheet).

We agree with this comment and we modified the text accordingly taking into account that during the LGM the Belluno valley hosted the Piave glacier about 800 m thick up to an elevation of about 1150 m

Line 401: this is age is unreliable, the deglaciation in the Piave catchment occur after 18-17 ka, see Pellegrini et al. (2005) and Carton et al. (2009). At 10 ka valley glaciers were already waned. The collapse of the Alpine glaciers was fast but it occurred at 18-17 ka as reported also by Ravazzi et al. (2014) and Rossato and Mozzi (2016).

We understand the point, but we set up this simple model just to estimate a first order of possible uplift rate due to the melting of this glacier. Since the more recent time estimates are older than the age we choose, at most, the true uplift rates would be lower than those estimated by the model, that already predicts modest glacial isostatic uplift rates. In light of your comment we add this sentence in the manuscript: "This is an upper bound estimate since recent studies (Pellegrini et al., 2005; Carton et al., 2009) evaluate the complete disappearance of the glacier occurred likely before 15 ka BP."

References, **in bold those used and to be added in our list**

Benedetti, L., Tapponnier, P., King, G. C., Meyer, B., & Manighetti, I. (2000). Growth folding and active thrusting in the Montello region, Veneto, northern Italy. Journal of Geophysical Research, 105(B1), 739–766.

Carton, A., Bondesan, A., Fontana, A., Meneghel, M., Miola, A., Mozzi, P., Primon, S. & Surian, N. (2009). Geomorphological evolution and sediment transfer in the Piave River watershed (north-eastern Italy) since the LGM. Géomorphologié: Relief. Process. Environ. 3, 37–58.

Clark, P. U., Dyke, A. S., Shakun, J. D., Carlson, A. E., Clark, J., Wohlfarth, B., Mitrovica, J. X., Hostetler, S. W. & McCabe, A. M. (2009). The Last Glacial Maximum. Science 325, 710–714.

Clark, P.U., Shakun, J.D., Baker, P.A., Bartlein, P.J., Brewer, S., Brook, E., Carlson, A.E., Cheng, H., Kaufman, D.S., Liu, Z., Marchitto, T.M., Mix, A.C., Morrill, C., Otto- Bliesner, B.L., Pahnke, K., Russell, J.M., Whitlock, C., Adkins, J.F., Blois, J.L., Clark, J., Colman, S.M., Curry, W.B., Flower, B.P., He, F., Johnson, T.C., Lynch-Stieglitz, J., Markgraf, V., McManus, J., Mitrovica, J.X., Moreno, P.I. & Williams, J.W. (2012). Global climate evolution during the last deglaciation. Proc. Natl. Acad. Sci. 109 (19), E1134–E1142.

Fontana, A., Mozzi, P., & Bondesan, A. (2008). Alluvial megafans in the Veneto-Friuli Plain: Evidence of aggrading and erosive phases during Late Pleistocene and Holocene. Quaternary International, 189(1), 71–90.

Fontana, A., Mozzi, P., & Marchetti, M. (2014). Alluvial fans and megafans along the southern side of the Alps. Sedimentary Geology, 301, 150–171.

Ivy-Ochs, S. (2015). Glacier variations in the European Alps at the end of the last glaciation. Cuadernos de Investigación Geográfica 41, 295– 315.

Monegato, G., Scardia, G., Hajdas, I., Rizzini, F. & Piccin, A. (2017). The Alpine LGM in the boreal ice-sheets game. Sci. Rep. 7, 2078.

Mozzi, P., 2005. Alluvial plain formation during the Late Quaternary between the southern Alpine margin and the Lagoon of Venice (northern Italy). Geografia Fisica e Dinamica Quaternaria (Suppl. 7), 219–230.

Pellegrini, G.B., Albanese, D., Bertoldi, R. & Surian, N. (2005). La deglaciazione alpina nel Vallone Bellunese, Alpi meridionali orientali. Geografia Fisica e Dinamica Quaternaria. Supplemento 7, 271–280.

Ravazzi, C., Pini, R., Badino, F., De Amicis, M., Londeix, L. & Reimer, P. (2014). The latest LGM culmination of the Garda Glacier (Italian Alps) and the onset of glacial termination. Age of glacial collapse and vegetation chronosequence. Quat. Sci. Rev. 105, 26–47.

Rossato, S. & Mozzi, P. (2016). Inferring LGM sedimentary and climatic changes in the southern Eastern Alps foreland through the analysis of a 14C ages database (Brenta megafan, Italy). Quaternary Science Reviews, 148, 115-127.

Rossato, S., Carraro, A., Monegato, G., Mozzi, P., & Tateo, F. (2018). Glacial dynamics in pre-Alpine narrow valleys during the Last Glacial Maximum inferred by lowland fluvial records (northeast Italy). Earth Surface Dynamics, 6, 809-828.

New insights into active tectonics and seismogenic potential of the Italian Southern Alps from vertical geodetic velocities

Letizia Anderlini[1*], Enrico Serpelloni[2], Cristiano Tolomei[2], Paolo Marco De Martini[2], Giuseppe Pezzo[2], Adriano Gualandi[3], Giorgio Spada[4]

[1] Istituto Nazionale di Geofisica e Vulcanologia, Bologna (Italy)
[2] Istituto Nazionale di Geofisica e Vulcanologia, Rome (Italy)
[3] Jet Propulsion Laboratory, California Institute of Technology (USA)
[4] DiSPeA, Urbino University (Italy)

Correspondence to: Letizia Anderlini (letizia.anderlini@ingv.it)

Abstract. This study presents and discusses horizontal and vertical geodetic velocities for a low strain-rate region of the Southalpine thrust front in northeastern Italy obtained by integrating GPS, InSAR and leveling data. The area is characterized by the presence of sub-parallel, south verging thrusts, whose seismogenic potential is still poorly known. Horizontal GPS velocities show that this sector of the Eastern Southern Alps is undergoing ~1 mm/a of NW-SE shortening associated with the Adria-Eurasia plate convergence, but the horizontal GPS velocity gradient across the mountain front provide limited constraints on the geometry and slip-rate of the several sub-parallel thrusts. In terms of vertical velocities, the three geodetic methods provide consistent results showing a positive velocity gradient, of ~1.5 mm/a, across the mountain front, which can be hardly explained solely by isostatic processes. We developed an interseismic dislocation model, whose geometry is constrained by available subsurface geological reconstructions and instrumental seismicity. While a fraction of the measured uplift can be attributed to glacial and erosional isostatic processes, our results suggest that interseismic strain accumulation at the Montello and the Bassano-Valdobbiadene thrusts are significantly contributing to the measured uplift. The seismogenic potential of the Montello thrust turns out to be smaller than that of the Bassano-Valdobbiadene fault, whose estimated parameters (LD = 9.1 km and slip-rate = 2.1 mm/a) indicate a structure capable of potentially generating a Mw > 6.5 earthquake. These results demonstrate the importance of precise vertical ground velocity data for modeling interseismic strain accumulation in slowly deforming regions, where often seismological and geomorphological evidence of active tectonics is scarce or not conclusive.

1 Introduction

Diffuse deformation, slow tectonic rates and long repeat times of large earthquakes make the estimate of seismic hazard at continental plate boundaries a challenging task. This is the case of the Italian Alps, a classic example of a broadly deforming continental collisional belt (Schmid et al., 2004). Present-day convergence between the Adriatic and Eurasian plates is largely accommodated in the Eastern Southern Alps, (ESA) (e.g. D'Agostino et al., 2005; Cheloni et al., 2014),

where the Adriatic lithosphere underthrusts the Alpine mountain belt. This area is characterized by a notable seismic risk, due to the high seismic hazard of northeastern Italy (*http://zonesismiche.mi.ingv.it*), high population density and widespread industrial activities. Geodesy indicates that the highest present-day deformation rates are localized along the mountain front of the Italian ESA (D'Agostino et al., 2005; Bechtold et al., 2009; Cheloni et al., 2014; Serpelloni et al. 2016), which is also the locus of several M>6 earthquakes (Rovida et al., 2015). For the Venetian sector of the ESA (between the Schio-Vicenza line and the Cansiglio plateau; see Fig. 1), however, historical and instrumental earthquake records indicate a lower seismic moment release rate with respect to its easternmost (Friuli) sector (Serpelloni et al., 2016). Here, discrepancies between geodetic and seismic deformation rates have been interpreted as due to partial locking of the ESA thrust front (Cheloni et al., 2014; Serpelloni et al., 2016). However, despite geological or geomorphological evidence of Quaternary deformation (Benedetti et al., 2000; Galadini et al., 2005), the identification of active faults responsible for large past earthquakes is not conclusive. **This area is also affected** ~~The same area is interested~~ by non-tectonic deformation transients associated with the hydrological cycle in karst regions and precipitations, which are well tracked and described by continuous GPS stations (Devoti et al., 2015; Serpelloni et al., 2018). These deformation transients, which mainly affect the horizontal components of ground displacements, make the estimate of the long-term horizontal tectonic deformation rates more challenging.

Overall, in the European Alps vertical GPS velocities correlate with topography (Serpelloni et al., 2013; Sternai et al., 2019), with widespread uplift at rates of up to ~2.0-2.5 mm/a in the North Western and Central Alps and ~1 mm/a across a continuous region from the Eastern to the South-Western Alps. Proposed mechanisms of uplift include the isostatic response to the last deglaciation **(19-11 Ka BP, Clark et al., 2012)**, long-term erosion, detachment of the Western Alpine slab, as well as lithospheric and surface deflection due to sub-Alpine asthenospheric convection (Serpelloni et al., 2013; Chery et al., 2016; Nocquet et al., 2016). In the study area the isostatic response to last deglaciation and long-term erosion are characterized by long-wavelength sub-mm/a patterns (e.g., Sternai et al. 2012; Serpelloni et al., 2013), whereas the elastic response to present deglaciation (Barletta et al., 2006~~; Spada et al., 2009~~) shows localized peaks of uplift (up to the mm/a scale) far from the study area. In the Eastern Alps, active shortening contributes to the observed uplift, but the pattern and amount of tectonic uplift due to elastic strain accumulation at faults is still unknown.

In the study area ~1 mm/a of SE-NW shortening is accommodated in ~40 km (Serpelloni et al., 2016), with the largest part being accommodated across the southernmost Thiene-Bassano-Cornuda, Montello and Cansiglio thrust faults (Cheloni et al., 2014; Serpelloni et al., 2016). However, horizontal GPS velocities in the Montello and Cansiglio areas appear "noisy", providing a poor fit to a single-fault model than in the Friuli sector of the ESA front (Cheloni et al., 2014; Serpelloni et al., 2016). Barba et al. (2013) used a sparse GPS velocity field for the Alps and vertical rates from precise leveling measurements performed by the Istituto Geografico Militare (IGM; IGM-RG, 1978) in the 1952-1984 time interval, over a distance of ~100 km from the Venetian plain to the Southern Alps mountain belt. The leveling measurements show a change from negative to positive vertical rates from the Venetian plain toward the mountains, which has been interpreted by Barba et al. (2013) as associated with elastic locking of the BVT. However, the leveling line does not cross the Bassano-Valdobbiadene thrust (BVT), passing partially through the Montello thrust (MT) and then running along the Fadalto Valley

(see Fig. 2), which is interpreted by Serpelloni et al. (2016) as an active left-lateral tectonic feature, separating the Carnic from the Dolomitic Alps.

In this work we integrate InSAR and GPS ground motion rates measurements across the MT and the BVT, the southernmost portion of the ESA south-verging fold-and-thrust belt (Fig. 1), with the goal of determining a new spatially dense 3D interseismic velocity field, considering also the available IGMI leveling measurements. We use two InSAR velocity fields obtained from ENVISAT satellite acquisitions along both ascending and descending orbits during the 2004-2010 and a GPS velocity field obtained from the analysis of data from continuous and semicontinuous stations between 1998 and 2018, with most of the GPS stations in the study area active after 2005. The datasets and the procedures used to analyze and integrate the geodetic observations are described in Section 3. In order to provide insight into the origin of the geodetic uplift we developed a two-dimensional dislocation model, jointly inverting GPS, leveling and InSAR velocities along a NNW-SSE oriented profile crossing the MT and BVT, as described in Section 4. The results are presented in Section 5 and discussed in Section 6.

2. Tectonic Setting

The South Alpine belt, which is part of the Alpine, Carpathian, Dinaridic system (AlCaDi after Schmidt et al., 2008), is a SSE-vergent orogenic system formed during Neogene time by indenting one continent into another (continent-continent collision). Within this model, the rigid Adriatic microplate has indented obliquely into a softer region along the southern margin of the European plate (Ratschbacher, et al., 1991a, 1991b; Frisch et al., 1998). This indenter model is consistent with the overall geometry of the Eastern Alps, with the region of maximum horizontal shortening being located north of the indenter front and with long, orogen-parallel structures that fan out toward the east and extrude the orogen eastward, toward the Pannonian Basin. The topography of the Eastern Alps also reflects the indenter tectonics causing crustal shortening, surface uplift and erosional response (Robl et al., 2017). The present-day convergence between the Adriatic and Eurasian plates is largely accommodated in the ESA, where the Adriatic lithosphere underthrusts the Alpine mountain belt. From Serpelloni et al. (2016), the Adriatic microplate rotates counterclockwise at ~0.3 °/Myr around a pole of rotation located in the western Po Plain of Italy, implying rates of convergence between Adria and Eurasia between 1.5 and 2.0 mm/a in the study region (Fig. 1).

The Southern Alps are a typical example of a deformed passive continental margin in a mountain range (Bertotti et al., 1993). Until the Oligocene, this Adriatic domain was the gently deformed retro-wedge hinterland of the Alps, intensively reworked only at its eastern boundary by the Paleogenic Dinaric belt. From the Neogene (~23 Ma), the Southalpine fold-and-thrust belt developed and progressively propagated toward the Adriatic foreland, mainly reactivating Mesozoic (~250–65 Ma) extensional faults (Castellarin et al., 1992). The study area (dashed box in Fig. 1) is located in the Venetian Southern Alps, which are part of the SSE-verging fold-and-thrust belt of the Southern Alps. Here the geometry of the fold-and-thrust belt is that of an imbricate fan, with a shortening of 30 km at least (Doglioni, 1992; Doglioni, 2003). The main thrusts are,

from the internal parts to the foreland, the Valsugana thrust (VS in Fig. 1), the Belluno thrust (BL in Fig. 1) and the Bassano-Valdobbiadene thrust (BVT in Fig. 1), the latter being associated with a morphological relief of ~1200 m above the plain (Fig. 3), known as Pedemountain flexure. The ESA southernmost front is now mainly buried beneath the alluvial deposits of the Venetian plain and sealed by Late Miocene to Quaternary (~ 7–2.5 Ma) deposits (Fantoni et al., 2002), and consists in the Thiene-Bassano-Cornuda thrust (TBC in Fig.1) and the MT (Benedetti et al., 2000; Fantoni et al., 2002; Galadini et al., 2005; Burrato et al., 2008; Danesi et al., 2015; MT in Fig. 1). The Montello hill (see Fig. 3) is generally interpreted as an actively growing ramp anticline on top of an active, north dipping, thrust that has migrated south of the mountain into the foreland (Benedetti et al., 2000). Benedetti et al. (2000) suggested that the Piave river changed its course because of the growth of the Montello hill, at a rate of 0.5 mm/a to 1.0 mm/a estimated from the ages of the river terraces. Modeling the deformation of the river terraces as a result of motion on the thrust ramp, Benedetti et al. (2000) estimated a constant slip rate of 1.8-2.0 mm/a.

The ESA mountain front and foreland is the locus of several $M \geq 6$ earthquakes (green squares in Fig. 1) in the last 2000 years (Rovida et al., 2016), but most of the seismogenic faults associated with these large earthquakes are still debated (Database of Italian Individual Seismogenic Sources, DISS; http://diss.rm.ingv.it/diss). Nevertheless, there is a general consensus for some of these earthquakes that the fault sources belong to the southernmost thrust fault system, emerging at the boundary between the Venetian plane and the mountain front (Benedetti et al., 2000; Galadini et al., 2005; Burrato et al., 2008; Cheloni et al., 2014). Information from historical sources and modern earthquake catalogues show that at least 12 earthquakes with $M \geq 6$ occurred in the past thousand years in the Italian Southern Alps. The last one (Mw 6.4) took place in 1976 in Friuli with several strong aftershocks ($5.1 \leq M_l \leq 6.1$) occurred in the following months (Slejko et al., 1999; Pondrelli et al., 2001). The largest earthquake in the study area is the 1695 Asolo earthquake, which is estimated, from the interpretation of historical information, as a ~Mw 6.4 event. However, the seismogenic source of this important earthquake is still uncertain. Uncertainties on the location, geometry and seismic potential of active faults in the Venetian Southern Alps persist due: i) to the complex structural framework of the region, inherited by the geodynamic evolution and resulting in deformation distributed over a vast area, ii) slow deformation rates along mainly blind faults, iii) sparse instrumental seismicity, causing some areas where strong historical earthquakes occurred to appear presently almost aseismic (Fig. 1).

3. Geodetic Observation

3.1 Global Positioning System Data

We use data from all the continuous GPS (cGPS) stations available for the study region provided by public institutions and private companies, integrated by data from a denser semicontinuous (sGPS) network installed by INGV from 2009 in the Venetian Southern Alps (Danesi et al., 2015). The solution presented here is part of a wider Euro-Mediterranean geodetic solution, including ~3000 cGPS stations that are analyzed in several sub-networks, and later combined.

The GPS velocities have been estimated analyzing the position time series, realized in the IGb08 reference frame, of all stations having an observation time span longer than 5 years (in the 1998.0-2017.5 time span, in order to be consistent with IGS08 products and the reference frame), in order to minimize possible biases in the linear trend estimation due to seasonal signals (Blewitt and Lavallée, 2002) and non-seasonal hydrological deformation signals (Serpelloni et al., 2018). The daily position time series were obtained analyzing raw data with the GAMIT/GLOBK (version 10.60; Herring et al., 2015) and QOCA (*http://qoca.jpl.nasa.gov*) software, following the three-step procedure described in Serpelloni et al. (2006, 2013). Details on the GPS data processing and post-processing are provided in the **Supplement** ~~supplementary material~~, and the reader is also referred to Serpelloni et al. (2013, 2016, 2018). The horizontal and vertical GPS velocities are provided in Table S1 of the **Supplement** ~~supporting material~~. Figure 2 shows the horizontal GPS velocities (black arrows, with 95% confidence error ellipses) in a Adria-fixed reference frame, using the rotation pole from Serpelloni et al. (2016), which has been calculated in a consistent IGb08 reference frame. The colored circles and diamonds, instead, show the vertical GPS and leveling rates, respectively, with white symbols representing stable sites (rates within ±0.5 mm/a), blue and red symbols representing points with negative (subsidence) and positive (uplift) rates, respectively.

Horizontal velocities show that the Veneto-Friuli plain is stable to within ±0.3 mm/a (see Fig. 2 and Table S1) with respect to the Adriatic microplate, whereas the ESA move toward SSE, orthogonal to the main thrust front, at rates slower than 2 mm/a. Figure 3 shows a velocity cross-section, with topography and seismicity, obtained projecting horizontal (Adria-fixed) GPS velocities along a NNW-SSE profile, highlighting the ~1 mm/a shortening accommodated between the Venetian plane and the Dolomites. Consistently with results from Serpelloni et al. (2016), the area where most of the shortening is accommodated, and the horizontal-strain rate is higher, corresponds to the southernmost thrust front (i.e. the MT, in this area). Regional kinematic models (Cheloni et al., 2014 and Serpelloni et al., 2016) show that part of the shortening across the southernmost ESA thrust front is likely accommodated by aseismic slip, although the spatial resolution of coupling maps are still poor. The horizontal velocity gradient across the Mt Grappa - Mt Cesen anticline is noisy, providing limited constraints on the presence of multiple locked faults across the mountain range.

Importantly, GPS and leveling vertical velocities coherently highlight a change from negative rates in the Venetian plain, near the Adriatic coastlines, to positive rates (up to ~1.9 mm/a) north of the Mt Grappa-Mt Cesen anticline (Fig. 2). Vertical velocities from leveling measurements refer to elevation changes measured during two campaigns in 1952 and 1984 by the Istituto Geografico Militare Italiano, IGMI (see the Supplement~~ary Material~~ for additional information), suggesting that the measured uplift is a steady feature over time-scales longer than the GPS observational time span. In section 3.4 this vertical velocity gradient is better detailed and discussed.

3.2 Synthetic Aperture Radar Data

We use Synthetic Aperture Radar (SAR) images (C-band sensor) acquired between 2004 and 2010 by the ENVISAT satellite, operated by the European Space Agency, along both ascending and descending orbits (Fig. 2). The displacement time-series and the mean ground velocities, in the line of sight (LOS) of the satellite geometry, have been

obtained adopting the SBAS multitemporal InSAR technique (Berardino et al., 2002). **The InSAR data processing has been performed using the SARScape module of ENVI software (http://sarmap.ch/tutorials/sbas_tutorial_V_2_0.pdf) to perform SBAS analysis.** The SBAS algorithm is based on a combination of many SAR differential interferograms that are generated by applying constraints on the temporal and perpendicular baselines. The inversion of the interferometric phase, performed with a Singular Value Decomposition (SVD) **algorithm**, produces a ground displacement time series for each coherent pixel, by minimizing possible topographic, atmospheric and orbital artifacts; the achieved accuracy of the displacements can be up to ~1 mm (Ferretti et al., 2007). In case of tropospheric delays correlated with topography , we accounted for them as a phase term linearly correlated with elevation. In **case of** ~~particular, when~~ tropospheric delays correlated with topography**, we** ~~are~~ accounted for **them**~~, they are modelled~~ as a phase term linearly correlated with elevation. The scaling coefficient is estimated directly from SAR interferograms, using a network approach, i.e., exploiting the redundancy of the interferometric pairs to derive a joint estimation for the scaling factor of each interferogram (Elliott et al., 2008; Wang and Wright, 2012; Jolivet et al., 2013). **Further details on the InSAR data processing and post-processing are provided in the Supplement.**

For descending and ascending orbits we analyzed 32 and 45 images, respectively (Table 1), selecting pairs of images applying constraints on the maximum orbital separation and the temporal distance between the two passages, in order to minimize spatial and temporal decorrelation effects. In particular, we chose 450 m and 600 days as the maximum values for the perpendicular and temporal baselines, respectively **(Fig. S1 of the Supplement)**. We use the 90-m Shuttle Radar Topography Mission (available at http://www2.jpl.nasa.gov/srtm) digital elevation model for the topography subtraction step (Farr et al., 2007). The analysis of both ascending and descending datasets has been performed applying a multi-looking factor equal to 20 for the azimuth, and 4 for the range direction, resulting in a final resolution of 90 m on the ground. **In order to avoid unwrapping issues and before the inversion steps, we checked each interferogram discarding all the pairs showing clear unwrapping errors and keeping the ones with low atmospheric noise.** Once the unwrapped phases inversion step is completed, the displacement time series (see the time span reported in Table 1) for each coherent pixel is obtained. Then the mean ground LoS velocities have been estimated fitting, with least-squares, a linear trend to the displacement time-series of each pixel. **We obtain for most of the pixels low values of Root Mean Squared Error and Chi-square (see Fig. S2 and S3 of the Supplement), indicating a mainly linear behavior for most of the dataset.** The mean error associated with the linear velocity estimate is ~1 mm/a.

Table 1. ENVISAT data set. Ground resolution values are obtained after a multi-looking operation.

Satellite	Orbit Type	Track	N. of used images	Number of pairs	Temporal span	Ground Resolution (m)	Incidence angle (°)
Envisat	Ascending	401	45	177	01/03/2004 11/10/2010	90	23

Envisat	Descending	394	32	125	06/12/2004 06/09/2010	90	23

3.3 GPS and InSAR integration method

The GPS and InSAR velocities have been compared projecting the three components of GPS velocities along the one-dimensional SAR satellite look direction **(see Fig. S4)**. The two datasets show a loose agreement in the velocity pattern ~~(see Fig. S1)~~ with some discrepancies between InSAR and GPS LoS rates (mainly at the border of the frames). These differences may be due to the different reference frame (that consists on a constant offset between the two datasets) and to residual orbital errors and long-wavelength atmospheric delays that are not completely removed from the InSAR mean velocity solution (e.g., Gabriel et al., 1989; Zebker et al., 1994). These last sources of errors are commonly represented by a bidimensional planar ramp in case of short strips acquisitions, i.e., 1-2 frames (Feng et al., 2012) like in our case, or a quadratic ramp for larger InSAR images (e.g. Lohman and Simons, 2005; Biggs et al., 2007).

The difference between InSAR and GPS velocities are commonly used to correct InSAR velocities and put both geodetic datasets in the same reference frame (e.g. Zebker et al., 1994; Hammond et al., 2010). In particular, we minimize the differences between GPS and InSAR LoS rates estimating and removing a ramp signal and a constant offset for the whole InSAR dataset. We use 11 and 9 GPS sites for the ascending and descending datasets, respectively, chosen among the sites with longer time-spans (>7 years) and as much as possible uniformly distributed over each SAR frame (see Fig. 4). The InSAR velocities, for comparison with GPS LoS rates, are estimated from averaging the values from a certain number of pixels around each of the selected GPS station, testing several radiuses of selection. The optimal radius of selection is defined as the one minimizing the misfit (evaluated in terms of root-mean-square error, RMSE) between GPS and InSAR LoS rates at the selected stations after the ramp removal (see Fig. **S5 in the Supplement**~~S2 in the supplementary material~~ for details). Before the correction, the RMSE deviation between GPS and InSAR data, for both the ascending and descending datasets, is of 1.15 mm/a and 0.83 mm/a, respectively. After the correction, the RMSE between GPS and InSAR datasets decreases to 0.55 mm/a and 0.63 mm/a for the ascending and descending datasets, respectively.

Figure 4 shows the corrected ascending and descending InSAR and GPS LoS velocities. The SE-NW (A-B in Fig. 4) cross sections show the overall good agreement in the LoS velocities between the two techniques. Both InSAR datasets show a positive velocity gradient of 2-3 mm/a in few tens of km across the BVT, and a common area of negative values of 1-2 mm/a in correspondence of the Venetian plain increasing toward the Adriatic coasts. Moreover, in the ascending dataset, we observe a small area with positive, but noisy, LoS velocities of ~1 mm/a across the Montello hill that are mostly within the mean uncertainty value of InSAR velocities. Figure 4 shows an area of positive LoS velocities in the northeastern corner of both the ascending and descending orbits, south of the Cansiglio plateau, which is more evident in the descending case. This area is located at the edge of both scenes and could be affected by errors associated with the orbital ramp estimation and removal during the processing chain (Berardino et al., 2002). In addition, during the filtering step (Goldstein et al., 1998, Ghulam et al., 2010) because the adopted moving window filter size was 64 pixels large, close to the frame border, where

less than 64 pixels remain, the presence of artifacts is possible. However, we cannot exclude that this positive signal may be of tectonic significance, being located near the mountain front where active thrust faults are present (Galadini et al., 2005), but the absolute values could be overestimated (as suggested by the disagreement between InSAR and GPS LoS rates near PORD) and cannot be considered reliable. Thus, we do not consider this signal in our analysis, which requires further investigations. Similarly, we excluded from the analysis the scattered pixels located in the northernmost sector of the ascending frame (Fig. 4), since they might be affected by unwrapping errors.

3.4 Integrated vertical velocity field

In order to estimate the vertical InSAR velocities we combine the ascending and descending LoS velocities assuming the N-S component as obtained from an interpolation of the GPS northward velocities in the area covered by the two ENVISAT frames. Given the namely near-polar sensor orbit direction, in fact, the N-S component of the InSAR velocities cannot be reliably derived. We calculate the East and Up components solving the following system of equations:

$$East = \Big((u2d/det) \times \big(Asc - (n2a * North)\big)\Big) - \Big((u2a/det) \times \big(Dsc - (n2d * North)\big)\Big)$$

$$Up = \Big((-e2a/det) \times \big(Asc - (n2a * North)\big)\Big) - \Big((e2a/det) \times \big(Dsc - (n2d * North)\big)\Big)$$

where *Asc* and *Dsc* are the ascending and descending LoS rates, *North* is the N-S interpolated component, *det = ((e2d * u2d) - (u2a * e2d)* and *u2d*, *e2d*, *n2d*, *u2a*, *e2a* and *n2a* are the descending and ascending direction cosines, respectively, which account for the LoS angle variability along the respective SAR images swath (Cianflone et al., 2015).

The vertical GPS and InSAR velocity field is shown in Fig. 5, together with vertical rates from the IGMI leveling measurements. Profile A-B runs normal to the strike of the MT and BVT faults, whereas the C-D profile runs along the leveling route (see the **Supplement and Fig. S6**~~supplementary material, Fig. S3,~~ for details about how uncertainties in the leveling rates are obtained). The three geodetic observations, which refer to different temporal intervals (1952-1984 for the leveling, 2004-2010 for SAR and ~2005-2017 for GPS data, respectively), show a good agreement in the vertical ground motion rates across the two profiles. The Venetian plain, near the coast of the northern Adriatic Sea show negative rates (e.g., station MSTR), which decrease toward north, being close to zero south of the Montello hill, across which a sub-mm/a uplift is apparent from Fig. 5, but not significant, considering the uncertainties and dispersion of the geodetic measurements. North of the Montello hill, GPS, InSAR, and leveling measurements coherently show a positive vertical velocity gradient, reaching in ~20 km positive rates up to 2 mm/a. However, while this vertical velocity gradient is rather well sampled by leveling data along the Fadalto Valley (profile C-D of Fig. 5), this is not the same across the Mt Grappa-Mt Cesen anticline, where a lack of InSAR observations is present due to the highly vegetated area of the Mt Cesen-Mt Grappa chain (profile A-B of Fig. 5).

Several studies investigated subsidence processes in the Venetian plain (e.g. Carminati and Di Donato, 1999; Carminati and Martinelli, 2002; Carbognin et al., 2004; Teatini et al., 2005; Bock et al., 2012), which is due to three main causes (both of natural and anthropogenic non-tectonic origin): 1- aquifer compaction after the strong

groundwater withdrawal in the second half of the last century (e.g. Gatto and Carbognin, 1981; Carbognin et al., 1995); 2- uncontrolled expansion of coastal settlements and industrial activities (e.g. Tosi et al., 2002); 3- recent sediment compaction (e.g. Brambati et al., 2003; Fontana et al., 2008). As we can see from the profile A-B of Fig. 5, subsidence rates increase from the center of the plain towards the coasts as due to the sum of the aforementioned processes. ~~Subsidence in the Venetian plain can be mainly ascribed to non-tectonic processes, such as sediment loading and residual sediments compaction (Carminati and Martinelli, 2002; Carminati et al., 2003; Teatini et al., 2005).~~ More localized faster subsidence (> 3 mm/a) is likely due to local anthropogenic processes, mainly associated with groundwater exploitation (e.g., the area between SUSE and VITT along the profile C-D of Fig. 5). Discrepancies between GPS rates and InSAR or leveling vertical rates (e.g., stations MT02, SUSE in Fig. 5) are likely due to known problems at GPS sites (e.g., MT02 monument has been destroyed and rebuilt in a different place two times) or the onset of recent processes, over the time interval of data availability, including anthropogenic processes (e.g., SUSE is located above a gas storage area: *https://www.edisonstoccaggio.it/it/campo-collalto* and its data quality and time-series is generally poorer than other sites). Although basically no InSAR observations are available along the Mt Grappa-Mt Cesen chain and on the Cansiglio Plateau the GPS stations there (i.e. MGRD, TAMB, CANV) show vertical positive rates that are less than 0.4 mm/a. Importantly, ~~the same~~ **these** stations are known to be **affected** ~~interested~~ by non-seasonal hydrological deformation due to pressurization of fractured karst aquifers (Devoti et al., 2015; Serpelloni et al., 2018), and their motion rates may be biased by these non-tectonic, non-seasonal, transient processes.

4. Dislocation Modeling

In order to interpret the horizontal and vertical velocity gradients across the MT and BVT faults we develop a two dimensional fault model, constructed from geologic cross sections, seismicity and geophysical prospections (see Fig. 3). The interseismic strain accumulation is represented by slip on buried rectangular dislocations, embedded in an elastic homogeneous half-space (Okada, 1985) with a Poisson ratio of 0.25. The length of the dislocations along strike is kept long enough to avoid edge effects and the width along the dip direction is exaggerated for the deepest fault in order to mimic the far-field long-term convergence rate. This approach has been widely used to simulate interseismic deformation associated with intracontinental thrust faults (e.g., Vergne et al., 2001; Hsu et al., 2003; Grandin et al., 2012; Tsai et al., 2012; Daout et al. 2016).

We perform an inversion of the geodetic velocities on a pre-determined fault geometry (see Fig. 6), composed by: a ramp-décollement system pertaining to the Montello thrust faults (MT), which is constrained by recent instrumental seismicity (Romano et al., 2019; Fig. 3) and focal mechanisms (Anselmi et al., 2011; Danesi et al., 2015), a fault ramp representing the Bassano-Valdobbiadene thrust (BVT), which is not well depicted by instrumental seismicity but better constrained by geological and geophysical interpretations (e.g. Galadini et al., 2005; Fantoni and Franciosi, 2010; see also Fig. 3), which both connect at depth along a single deeply rooted thrust, which is extended downdip (Castellarin et al.,

2006). We keep fixed the strike, perpendicular to the horizontal shortening rate direction (i.e. 65°N, see Fig. 2), the northward dip angles (see Fig. 6 for details), and the fault positions, while only for the Montello décollement and the deeper ramp the width has been kept constant. Assuming this fault geometry, we invert the geodetic velocities for determining two locking-depth (LD) values, that is the depth of the upper edge of the dislocation, indicating the shallow locked seismogenic fault portion for the MT and BVT ramps, and the dip-slip rates of all the fault segments (see Fig. 6).

The inversion method exploits a constrained, non-linear, derivative-based optimization algorithm (i.e. interior-point, see Byrd et al., 1999; Waltz et al., 2006). It allows to estimate the optimal parameter solution corresponding to a possible global minimum of the cost function, representing the misfit between the model prediction and the geodetic measurements. These algorithms depend on the gradient and higher-order derivatives in order to guide them through misfit space, thus they can get trapped in a local minimum (Cervelli et al., 2001), providing the best results when the starting point is near the global minimum. However, in order to ensure that we find a global solution in the inversion, we tested several different initial guess founding always the same model estimate. The cost function to be minimized is ~~The inversion method exploits a constrained, non-linear, optimization algorithm (Celis et al., 1984; Árnadóttir and Segall, 1994) that follows the approach of Johanson and Bürgmann (2005). It allows to estimate the set of fault parameters corresponding to a global minimum of the misfit between the model prediction and the geodetic data, evaluated by~~ the weighted residual sum of squares:

$$WRSS = (d_{obs} - d_{mod})^T \times cov^{-1} \times (d_{obs} - d_{mod}) \quad (1)$$

where *cov* is the covariance matrix of geodetic data errors, and $d_{mod} = \boldsymbol{G}(m)$, as $\boldsymbol{G}$ is the Green's function matrix depending on the fault geometry and slip parameters, m (Okada, 1985). **The data covariance matrix *cov* is computed as follows: $cov = \Sigma R \Sigma^T$, where Σ is the diagonal matrix of data uncertainty and R is the data correlation matrix, that is dimensionless, equal to one along the diagonal and the off-diagonal elements representing the correlation between each couple of data. Assuming the three geodetic dataset (GPS, InSAR and leveling) independent among them, the whole covariance matrix is composed by three independent blocks, one for each dataset. The correlation values are nonzero only for the three components of each GPS site, considering the measurements obtained by the GPS stations to be uncorrelated among them, and for the leveling data, following the approach of Árnadóttir et al. (1992). The InSAR data covariance matrix is instead diagonal with equal variance of 1 $mm^2/year^2$ for all the pixels.** The locking depths have been forced **by the inversion algorithm** to be within the seismogenic layer, as defined by instrumental seismicity (Fig. 3), while the dip-slip rates have been constrained to be kinematically consistent along the four fault planes. The latter constraint imposes the conservation of the horizontal and vertical motion along the fault junctions, by means of the geometric relationships proposed by Daout et al. (2016).

In the inversion we use horizontal and vertical velocities of 15 GPS sites (highlighted in Table S1 of the **Supplement** ~~supplementary material~~) located within a 35 km wide profile crossing the MT and BVT faults along a -25°N direction (dashed box of Fig. 2, perpendicular to the strike direction of the faults), selecting those stations reliable for site

stability. We invert InSAR LoS rates from both ascending and descending datasets (corrected of the planar ramp), exploiting the completeness of information provided by the LoS velocities, containing both the horizontal and the vertical contributions.

InSAR velocities within the same swath profile used to select GPS stations have **been** subsampled in order to reduce the density of pixels while maintaining the first order ground deformation information (**Fig. S7**~~see the supplementary material for the subsampling method and Fig. S4~~) and allowing for reasonable computational costs. **Most of studies, performing a subsampling of InSAR data for geophysical inversions, use the quadtree sampling method (e.g. Jónsson et al., 2002; Pedersen et al., 2003; Lohman and Simons, 2005; Jolivet et al., 2012; Maurer and Johnson, 2014) that allows to reduce the number of data in order to represent the statistically significant portion of the displacement signal (Jónsson et al., 2002). In our case, with low deformation gradients it is highly risky to apply a subsampling method that depends on the deformation signal itself. For this reason we apply an alternative method that uniformly reduce the density of pixels and the specific technical details are provided in the Supplement.** The final number of InSAR data has been reduced to less than 3000 points for each dataset (see Table S3 of the **Supplement**~~supporting material~~). The resampled pixels with mean ground velocity less than -0.5 mm/a are excluded from the modeling, assuming that subsidence **is** ~~can only be~~ due to non-tectonic processes that **we cannot take into account in this analysis (see Section 3.4)**. The total number of resampled InSAR data (joining ascending and descending together) used during the inversion counts 3115 pixels. We jointly invert also the whole leveling dataset (see Table S2), calculating the associated covariance matrix as described in Árnadóttir et al. (1992), and excluding from the inversion the leveling points with vertical velocities less than -0.5 mm/a for the same reason mentioned above.

Given the larger number of InSAR velocity data, compared to the GPS and leveling ones, we apply a relative weight, *Wsar* (varying between 0 and 1), that rescales the InSAR covariance matrix. This approach allows to calibrate the relative importance of the InSAR dataset with respect to the others, aiming at finding the model that can best reproduce all the geodetic observations. The optimal value of *Wsar* (equal to 0.46) has been chosen as the "knee point" of the trade-off curves between the WRSS (Eq. 1) of GPS and InSAR data, and the WRSS of leveling and InSAR data, as the factor *Wsar* varies (see Fig. **S8 in the Supplement**~~S5 in the supplementary material~~ for details). Although the weighting factor affects the InSAR covariance matrix during the inversion, the trade-off curves analysis has been performed considering the original covariance matrix of InSAR data.

5. Results

The estimated model parameters (locking depths and dip-slip rates), with their uncertainties, and residuals in terms of RMSE are reported in Table 2. Figure 7 shows the measured and modeled horizontal and vertical geodetic velocities, as well as the InSAR ascending and descending LoS rates. **The error bounds for the estimated optimal fault parameters have been evaluated using the bootstrap method (e.g. Efron and Tibshirani, 1986; Árnadóttir and Segall, 1994) with 1000 random resampling of data. The bootstrap procedure allows us to estimate confidence intervals of the derived**

parameters (Segall and Davis, 1997) without making assumptions about the underlying statistics of errors (Amoruso and Crescentini, 2008), reflecting the limitations of the used data set (Cervelli et al., 2001). Figure S9 in the Supplement shows the frequency distribution of the optimal fault models after the bootstrap procedure, reporting corresponding 95 percentile confidence bounds (reported in Table 2) by means of the percentile method, and the trade-off distributions between fault parameters pairs. ~~Due to the linear dependence between velocities and slip rates, the slip rate errors have been determined from the *a posteriori* model covariance matrix. On the contrary ground displacement rates depend nonlinearly on locking depth (LD) parameters, so their uncertainties have been evaluated using the bootstrap method (e.g. Efron and Tibshirani, 1986; Árnadóttir and Segall, 1994) with 1000 data samples, defining the 68% and the 95% confidence bounds (see Fig. S6 in the supplementary material for the frequency distributions) by means of the percentile method.~~

The inversion results show that the Bassano Valdobbiadene thrust is characterized by a greater locking depth (LD = 9.1 km) and a faster dip-slip rate (2.1 mm/a) than the Montello ramp fault (LD = 5.6 km, SR = 0.5 mm/a). Moreover, the locking depth of the Bassano Valdobbiadene thrust is better constrained by the data than the one estimated for the Montello ramp, which is weakly constrained because of the noisy sub-mm geodetic signal (close to the geodetic techniques limits) measured above the structure, to which the fault geometry is more sensitive. The trade-off distributions between parameter pairs (Fig. S9) show that the locking depth estimates have no correlation with the other parameters, while the dip-slip rates have strict correlations among them due to the kinematic conservation constraint. The only slip-rate parameter we can consider independent is the deep ramp slip rate (SRDD, Fig. 6) representative of the far field convergence rate, and for which we obtain the widest confidence bounds (Table 2). The obtained results point out that the surface velocity gradient is mostly explained by the BVT ~~whose fault parameters are better constrained by the geodetic data (see Table 2 and Fig. S6)~~, thus suggesting a greater seismogenic potential than that one expected for the Montello thrust fault.

The fault model overall reproduces the observed velocity gradients from all datasets (see Fig. 7), although we find a partial discrepancy between the leveling data and the modeled vertical velocity field (Table 2, Fig. 7). This misfit may be due to the fact that the leveling line from the Montello hill runs along the Fadalto valley (see Fig. 2) and those points might be sensitive to a deformation signal associated with the Cansiglio thrust fault, located ~10 km south of the BVT (Galadini et al., 2005). In correspondence of the Belluno Valley (see Fig. ~~7~~6), both GPS and InSAR vertical rates show larger misfit with respect to the fault model. In particular, InSAR data show a steeper velocity gradient than that reproduced by the model, and this may be ascribed to some artifacts not totally estimated and removed during the SAR data processing, and likely due to the correlation between atmosphere and topography gradient (e.g. Elliott et al., 2008; Doin et al., 2009; Jolivet et al., 2012; Shirzaei and Bürgmann, 2012).

Table 2. Output model parameters (with 95~~1σ error bounds or 68~~ percentile confidence intervals) and data residuals in terms of Root Mean Squared Errors, RMSE.

LD Montello Ramp	LD Bassano Ramp	Slip rate Montello Ramp	Slip rate Montello Flat	Slip rate Bassano Ramp	Slip rate Deep Ramp	RMSE GPS	RMSE LEV	RMSE InSAR
$5.6_{-3.8}^{+3.5}$ km	$9.1_{-0.6}^{+1.3}$ km	$0.5_{-0.1}^{+0.2}$ ± 0.3 mm/a	0.4 ± 0.1 mm/a	$2.1_{-0.6}^{+0.8}$ ± 0.3 mm/a	$2.5_{-0.7}^{+0.8}$ ± 0.2 mm/a	0.44 mm/a	0.72 mm/a	0.66 mm/a

6. Discussion

Overall, our results are consistent with conclusions of Barba et al. (2013), who developed a 2D finite-element model constrained by the leveling vertical rates, showing that the amount of interseismic locking associated with the BVT must exceed that associated with the MT. The shallower locking depth estimated for the Montello ramp is also consistent with other inferences on interseismic fault coupling for the ESA front, constrained by GPS horizontal velocities, indicating the MT as partially elastically locked (Cheloni et al., 2014; Serpelloni et al., 2016).

The Bassano-Valdobbiadene fault is classified as seismogenic and capable of M_w ~6.5 earthquakes in the DISS, but its late Quaternary activity is debated. No major earthquakes are unequivocally associated with this fault (see Fig. 1). The larger seismic event here, the Mw 6.4, 1695 Asolo earthquake (see Fig. 1), is located at the foothills of the mountain range delimited by the BVT front, but is in general associated with the westernmost portion of the Montello thrust, the Bassano-Corduna segment (Galadini et al., 2005; Burrato et al., 2008). Only recently local seismic networks (Priolo et al., 2015) and temporary seismic experiments (Anselmi et al., 2011; Danesi et al., 2015) have improved the imaging of faults at depth, indicating earthquakes with thrust focal mechanisms for both the Montello and Bassano-Valdobbiadene faults (Fig. 3).

During the 70s and the 80s, a large amount of data on the Pliocene-Quaternary fault activity of NE Italy have been collected. Castaldini and Panizza (1991) classified the BVT as active (i.e., showing tectonic movements in the middle Pleistocene-Holocene time). They proposed an uplift rate up to 1 mm/a, based on evidence of deformation in Würmian deposits laying on structures associated with the BVT (Pellegrini and Zanferrari, 1980; Zanferrari et al., 1980), morphotectonic evidence of scarps aligned with the thrust, offsets recorded in karsified surfaces of Mindel-Riss age, and changes in the post-Würmian hydrography (Zanferrari et al., 1980). Galadini et al. (2001) draw an updated summary of the active faults **in the Eastern Southern Alps** (i.e., responsible for the displacements of deposits and/or landforms related or subsequent to the last glacial maximum, LGM, **set at 26-19 Ka BP at global scale following Clark et al., 2009, and more specifically at 25-21 Ka BP for the Alpine area as suggested by Monegato et al., 2017 and references therein). Galadini et al. (2001)** ~~occurred ~ 20 to 19 ka) in the Eastern Southern Alps. They~~ produced a map including the main faults whose length is consistent with the occurrence of earthquakes with M≥6.2 (based on the rupture length/magnitude relationship by Wells & Coppersmith 1994), where the BVT is represented as an unsegmented active fault from the Schio-Vicenza line to the Fadalto line. However, in the most recent literature (e.g., Galadini et al., 2005; Burrato et al., 2009; Moulin and Benedetti, 2018), evidence of recent activity of the BVT appears not conclusive. It is worth considering that the lack of evidence of recent displacements in the mountainous region may have been conditioned by the erosional-depositional

evolution of the Alps since the LGM. Intense erosion by the glacial tongues and subsequent rapid deposition of thick successions of alluvial deposits may have hidden the evidence of fault activity, making geomorphological evidence of recent tectonic activity debatable.

On the contrary, the recent deformation of the Montello thrust is testified by several Middle and Upper Pleistocene warped terraces of the Piave River paleo-course flanking the western termination of the fold (Benedetti et al., 2000 and references therein), and by the eastward deflection of the Piave River around the growing anticline. Benedetti et al. (2000) associated to the MT at least three earthquakes with M < 6 (778 A.D., 1268 and 1859), which have been however revised in the Italian macroseismic catalogue (Rovida et al., 2016).

Geological and geomorphological data appears thus not fully consistent with the geodetic deformation signals and the interpretation presented in this work. The slip-rate estimated for the flat and ramp portions of the Montello thrust are 0.4 ± 0.2 and 0.5 ± 0.3 mm/a, respectively. These values are smaller than those estimated from modeling the deformation of the river terraces by Benedetti et al. (2000), who estimated a constant slip-rate of 1.8-2.0 mm/a, values that are however incompatible with the sub-mm actual geodetic signal measured above the Montello hill. **A possible explanation for the high rate obtained by Benedetti et al., 2000, is related to the new chronologies proposed for the Alpine LGM (as old as 25 Ka BP, Monegato et al., 2017) and for the Montebelluna megafan (125-30 Ka BP, Mozzi, 2005; Fontana et al., 2014), much older than the data available in 2000.** The estimated slip-rate for the BVT (2.1 ± 0.3 mm/a) is much greater than the one reported in the DISS database (0.3-0.7 mm/a), inferred from regional tectonic and geological interpretations. To our knowledge, there are no other independent estimates of slip-rates for this fault, for which conversely our estimates are rather well constrained by a significant geodetic signal. Considering a length of ~30 km for each fault, a shear modulus of 24 GPa (as a mean value for the whole study region estimated from Vp and Vs values reported in Anselmi et al., 2011) and the estimated slip-rates and locking depths (Table 2), the maximum magnitude expected in 1000 years as recurrence time is a Mw = 6.9 for the BVT and a Mw = 6.2 for the MT. These values should be assumed as upper bounds because, given the simple model used, we do not take into account some complexities like the presence of lateral and vertical variations of fault geometry and rheological parameters, that may prevent the co-seismic rupture propagation, and partially coupled fault portions that can reduce the seismogenic potential.

Despite the fault model provides a satisfactory explanation of the geodetic velocity gradients, it is worth considering that the vertical component of motion may be influenced by further ongoing processes on an alpine spatial scale. Indeed, GPS data show that the Alps are undergoing widespread uplift at rates up to ~2-2.5 mm/a in the North-Western and Central Alps, and ~1 mm/a across a continuous region from the Eastern to the South-Western Alps (Serpelloni et al., 2013; Chen et al., 2018), highlighting a correlation with topography (Serpelloni et al., 2013). Proposed mechanisms of uplift include isostatic response to the last deglaciation, to the present ice melting and to erosion, detachment of the Western Alpine slab, as well as lithospheric and surface deflection due to mantle convection (see Sternai et al., 2019 for a review). The relative contribution of each proposed mechanism to the geodetically measured uplift is, however, difficult to estimate, but their total contribution is of the order of few tenths of mm/a (Sternai et al., 2019). **Moreover, it is also worth considering that models**

proposed to quantify these contributions (e.g. Barletta et al., 2006; Spada et al. 2009; Norton and Hampel, 2010; Sternai et al, 2012; Mey et al., 2016) are less reliable at the borders of the Alpine belt (Sternai et al., 2019), where our study area is located, making it even more speculative to apply a plausible "isostatic" correction to the actual uplift rates. The spatial patterns associated with the aforementioned processes have a characteristic wavelength of hundreds of km, and correcting for these contribution would slightly reduce the intensity of uplift rates, leaving the observed velocity gradient mostly unchanged. In order to evaluate the effects of "correcting" the actual vertical velocities for long wavelength isostatic contributions on slip-rate and locking-depth estimates, we remove a linear gradient of uplift rate along 100 km of distance from the measured geodetic rates. Despite being speculative and based on strong assumptions (see the Supplement for details), we can assume this approach as an upper-bound case to evaluate the impact of correcting or not for long-wavelength uplift signals on the inversion results. After the application of this correction, the locking-depth and slip-rate estimates are slightly reduced (see Figure S10 in the Supplement) without significant variations, resulting widely within the error bounds of the optimal fault parameters (Table 2) and leading to exactly the same seismogenic potential estimates for the MT and BVT faults. ~~The uplift pattern associated with the aforementioned processes has a characteristic wavelength of hundreds of kilometres, and a possible correction for these contributions would slightly reduce the intensity of uplift rates. If it were possible to apply such a correction, the slip-rates estimates on the fault planes could be slightly reduced, in turn decreasing a little the seismogenic potential associated with the MT and BVT faults.~~

As these long-wavelength processes could hardly explain the local vertical velocity gradient observed across the Venetian mountain front, a possible source of more localized uplift rate gradient in the study area may come from the contribution of local ice or from present-day glacier shrinkage. At the LGM the Belluno valley **hosted the Piave glacier up** ~~was filled by the Piave ice sheet~~ to an elevation of ~**1150**~~1000~~ m (**Pellegrini et al., 2005; Carton et al., 2009**)~~see e.g., Benedetti et al., 2000~~). Pellegrini and Zambrano (1979) have estimated a width of ~15 km for the ice pond, a length of ~45 km and a maximum thickness of 600-800 m. Given the spatial correlation between the fastest vertical geodetic velocities and the location of the former Piave ice pond, we have employed a simple isostatic model with the aim of providing a first-order estimate of the spatial pattern and range of magnitudes for the isostatic response to deglaciation of this local ice sheet. The isostatic response has been evaluated using the TABOO software (Spada et al., 2004, 2011), assuming a cap profile for the pond, an equivalent area of 45 x 15 km^2, a maximum thickness of 800 m **(Pellegrini et al., 2005)**, and an instantaneous deglaciation occurring 10 ka ago. **This is an upper bound case since recent studies (Pellegrini et al., 2005; Carton et al., 2009) evaluate the complete disappearance of the glacier occurred likely before 15 ka BP.** The Earth model includes an elastic crust and a mantle viscosity profile consistent with the ICE-5G(VM2) model of Peltier et al. (2004). Figure **S11 in the Supplement**~~S7 in the supporting material~~ shows how the expected vertical velocities due to the Piave ice melting are sensitive to the assumed crustal thickness. Assuming in this region a crustal thickness between 30 and 40 km (Molinari et al., 2015), the model predicts modest glacial isostatic uplift rates (~0.1 mm/a).

Although we acknowledge the importance of glacio-isostatic contributions to the present-day uplift of Eastern Southern Alps, the vertical velocity gradient identified by terrestrial and space geodetic measurements across the venetian mountain front is **mostly** ~~most likely~~ associated with active tectonic processes. Indeed, a simple elastic dislocation model based on seismological, geological and geophysical evidence can satisfactorily explain both the horizontal GPS velocities and the vertical GPS+InSAR+leveling rates, consistently. **However, important constraints from new seismicity data and new surface and subsurface geological observations will be required, together with denser GNSS data, to better constrain the tectonic rates and seismogenic potential in this area.**

7. Conclusions

We study the interseismic deformation at the Adria-Alps boundary in northeastern Italy, focusing on a sector of the Southern Alps fold-and-thrust belt, where WSW-ENE oriented sub-parallel, south-verging, thrusts presently accommodate ~1 mm/a of NW-SE shortening. Seismogenic faults databases indicate two possible sources for the larger historical earthquakes of the area: the Bassano-Valdobbiadene thrust (BVT), bordering the mountain front, and the Montello thrust (MT), buried beneath the alluvial venetian plain. Both GPS and InSAR measurements, consistently with precise leveling measurements, show a positive vertical velocity gradient from the Venetian plain toward the Alps, with the highest rates, of the order ot 1.5 mm/a, located ~20 km north of the mountain front. The three geodetic measurements span different time-periods from 1950 to the present day, suggesting that this uplift pattern is consistent over a longer time interval than the most recent GPS measurements.

We develop an interseismic fault model, constrained by InSAR, GPS and leveling rates, estimating slip-rates and locking depths of the BVT and MT faults, whose geometry is defined by geological and seismological data. This simple model satisfactorily explains both horizontal and vertical geodetic velocities, suggesting that both thrust faults are accumulating elastic strain. The higher locking-depth and slip-rate estimated for the BVT, which is required to explain the observed uplift rate gradient, point toward a higher seismogenic potential of this fault (compatible with a $Mw_{max} > 6.5$ in 1 Kyrs), accordingly to recent results indicating a limited interseismic locking for the MT frontal ramp.

This work demonstrates the important constraints that vertical ground velocity measurements can provide for interseismic deformation studies associated with thrust faults in slowly deforming regions, as already shown in other faster deforming convergent boundaries. More importantly, since several processes contribute to mountains uplift, with glacio-isostatic contribution being the greatest ones in the Alps, a more accurate estimate of the contribution of each process at local scale is necessary in order to correct the measured geodetic uplift for its non-tectonic components, guaranteeing a more reliable estimate of the geodetic slip-rates. From this point of view, the Eastern Southern Alps represent an ideal natural laboratory for further investigations.

Data availability. **GPS and leveling velocity data that support the findings of this study can be found in the Supplement. The InSAR line-of-sight velocities obtained in this work are available through the B2SHARE service within the European EUDAT infrastructure at: https://doi.org/10.23728/b2share.486d3b553c564cc6826e24548e85ad1d** ~~Data from the survey-mode GPS network can be obtained contacting ES. The InSAR data that support the findings of this study are available upon request from the corresponding author~~

Supplement. The supplement related to this article is available on-line at:

Author contributions. ES processed the GPS data, CT and GP processed the InSAR data and PMDM provides the leveling data. AG wrote the code for the InSAR data subsampling and LA developed the data analysis, integration and correction of all the datasets, and carried out the data modeling. GS developed the GIA analysis. LA, ES, CT and GS interpreted the results and wrote the article. All the authors have contributed in the article preparation.

Competing interests. The authors declare that they have no conflict of interest.

Acknowledgements. ~~This study has been developed in the framework of the project TRANSIENTI, founded by the Italian Ministry of Education, Universities and Research (MIUR) "Premiale 2014".~~ We are grateful to all public and private institutions and companies that make GPS data freely available for scientific applications. In particular, we acknowledge the EPN-EUREF network, Leica-ITALPOS, Topcon-NETGEO, ASI-GEODAF, INGV-RING, InOGS-FREDNET, Rete "Antonio Marussi" in Friuli Venezia Giulia, STPOS and TPOS in Trentino-Alto Adige and Regione Veneto, and the ARPAV-Belluno. Most of the figures have been created using the Generic Mapping Tools (GMT) software (Wessel & Smith, 1998). **Mario Anselmi is thanked for fruitful discussions about the modeling and the analysis of results. We thank Romain Jolivet, Giovanni Monegato and an anonymous reviewer for their constructive comments that allowed to improve this manuscript.**

Financial support. LA is supported by INGV-MISE-DMGS 2018-19 project. GS is funded by a FFABR (Finanziamento delle Attività Base di Ricerca) grant of MIUR (Ministero dell'Istruzione, dell'Università e della Ricerca) and by a DiSPeA research grant. **This study has been partially supported by the project TRANSIENTI, founded by the MIUR "Premiale 2014",** ~~This study was partially funded~~ by the Italian Presidenza del Consiglio dei Ministri, Dipartimento di Protezione Civile (Proj. S1 2013-2014 INGV- DPC Agreement), **and by the MIUR "Pianeta Dinamico" institutional project.** This paper does not necessarily represent an official opinion or policy of the Dipartimento di Protezione Civile.

References

Amoruso, A., Crescentini, L.: Inversion of synthetic geodetic data for the 1997 Colfiorito events: clues on the effects of layering, assessment of model parameter PDFs, and model selection criteria. Ann. Geophys., 51, doi:10.4401/ag-3027, 2008.

Anselmi, M., Govoni, A., De Gori, P., and Chiarabba, C.: Seismicity and velocity structures along the south-Alpine thrust front of the Venetian Alps (NE-Italy), Tectonophysics 513, 37–48, doi:10.1016/j.tecto.2011.09.023, 2011.

Árnadóttir, T., Segall, P., and Matthews, M.: Resolving the discrepancy between geodetic and seismic fault models for the 1989 Loma Prieta, California, earthquake, Bulletin of the Seismological Society of America, 82, 2248–2255, 1992.

Árnadóttir, T. and Segall, P.: The 1989 Loma Prieta earthquake imaged from inversion of geodetic data, Journal of Geophysical Research: Solid Earth 99, 21835–21855, doi:10.1029/94JB01256, 1994.

Barba, S., Finocchio, D., Sikdar, E., and Burrato, P.: Modelling the interseismic deformation of a thrust system: seismogenic potential of the Southern Alps, Terra Nova, 25, 221-227, doi: 10.1111/ter.12026, 2013.

Barletta, V.R., Ferrari, C., Diolaiuti, G., Carnielli, T., Sabadini, R., and Smiraglia, C.: Glacier shrinkage and modeled uplift of the Alps, Geophys. Res. Lett. 33, doi: 10.1029/2006GL026490, 2006.

Bechtold, M., Battaglia, M., Tanner, D.C., and Zuliani, D.: Constraints on the active tectonics of the Friuli/NW Slovenia area from CGPS measurements and three-dimensional kinematic modeling, J Geophys Res, 114, doi:10.1029/2008JB005638, 2009.

Benedetti, L., Tapponnier, P., King, G.C.P., Meyer, B., and Manighetti, I.: Growth folding and active thrusting in the Montello region, Veneto, northern Italy, Journal of Geophysical Research: Solid Earth, 105, 739–766, doi:10.1029/1999JB900222, 2000.

Berardino P., Fornaro G., Lanari R., and Sansosti E.: A new algorithm for surface deformation monitoring based on small baseline differential SAR interferograms, IEEE Trans. Geosci. Remote Sens., 40, 2375-2383, doi:10.1109/TGRS.2002.803792, 2002.

Bertotti, G., Picotti, V., Bernoulli, D., Castellarin, A.: From rifting to drifting: tectonic evolution of the South-Alpine upper crust from the Triassic to the Early Cretaceous, Sediment. Geol, 86, 53–76, doi: 10.1016/0037-0738(93)90133-P, 1993.

Biggs, J., Wright, T., Lu, Z., Parsons, B.: Multi-interferogram method for measuring interseismic deformation: Denali Fault, Alaska, Geophysical Journal International, 170, 1165–1179, doi:10.1111/j.1365-246X.2007.03415.x, 2007.

Blewitt, G. and Lavallée, D.: Effect of annual signals on geodetic velocity, J Geophys Res, 107, 2145, doi:10.1029/2001JB000570, 2002.

Bock, Y., Wdowinski, S., Ferretti, A., Novali, F., Fumagalli, A.: Recent subsidence of the Venice Lagoon from continuous GPS and interferometric synthetic aperture radar, Geochem. Geophys. Geosyst., 13, Q03023, doi:10.1029/2011GC003976, 2012.

Brambati, A., Carbognin, L., Quaia, T., Teatini, P., Tosi, L.: The Lagoon of Venice: Geological Setting, Evolution and Land Subsidence, Episodes, 26, 264-268, 2003.

Burrato, P., Poli, M.E., Vannoli, P., Zanferrari, A., Basili, R., and Galadini, F.: Sources of Mw 5+ earthquakes in northeastern Italy and western Slovenia: An updated view based on geological and seismological evidence, Tectonophysics, 453, 157–176, doi:10.1016/j.tecto.2007.07.009, 2008.

Byrd, R.H., Hribar, M. E., Nocedal, J.: "An Interior Point Algorithm for Large-Scale Nonlinear Programming," SIAM Journal on Optimization, Vol 9, No. 4, pp. 877–900, 1999.

Carbognin L., Tosi, L., Teatini, P.: Analysis of actual land subsidence in Venice and its hinterland (Italy). In: Barends J.F., et al. (1995, eds.) - Land Subsidence, 129-137, A. A. Balkema, Rotterdam, 1995.

Carbognin, L., Teatini, P., Tosi, L.: Eustacy and land subsidence in the Venice Lagoon at the beginning of the new millennium. J. Marine System, 51(1–4), 345– 353, doi:10.1016/j.jmarsys.2004.05.021, 2004.

Carminati, E., Di Donato, G.: Separating natural and anthropogenic vertical movements in fast subsiding areas: The Po plain (N. Italy) case, Geophys. Res. Lett., 26, 2291–2294, doi:10.1029/1999GL900518, 1999.

~~Carminati, E., Doglioni, C., and Scrocca, D.: Apennines subduction-related subsidence of Venice (Italy), Geophys. Res. Lett., 30, 1717, doi:10.1029/2003GL017001, 2003.~~

Carminati, E. and Martinelli, G.: Subsidence rates in the Po Plain, northern Italy: the relative impact of natural and anthropogenic causation, Engineering Geology, 66, 241–255, doi: 10.1016/S0013-7952(02)00031-5, 2002.

Carton, A., Bondesan, A., Fontana, A., Meneghel, M., Miola, A., Mozzi, P., Primon, S. & Surian, N.: Geomorphological evolution and sediment transfer in the Piave River watershed (north-eastern Italy) since the LGM. Géomorphologié: Relief. Process. Environ. 3, 37–58, 2009.

Castaldini, D. and Panizza, M.: Inventario delle faglie attive tra i fiumi Po e Piave e il lago di Como (Italia Settentrionale), Il Quaternario Italian Journal of Quaternary Sciences, 4(2), 333-410, 1991.

Castellarin A., Cantelli, L., Fesce. A.M., Mercier, J.L., Picotti, V., Pini, G.A., Prosser, G., and Selli L.: Alpine compressional tectonics in the Southern Alps. Relationships with the N-Apennines, Annales Tectonicae, 6, 62-94, 1992.

Castellarin, A., Vai, G.B., and Cantelli, L.: The Alpine evolution of the Southern Alps around the Giudicarie faults: A Late Cretaceous to Early Eocene transfer zone, Tectonophysics, 414, 203–223, doi:10.1016/j.tecto.2005.10.019, 2006.

Cervelli, P., Murray, M.H., Segall, P., Amelung, F., Aoki, Y., Kato, T.,: Estimating source parameters from deformation data, with an application to the March 1997 earthquake swarm off the Izu Peninsula, Japan, J. geophys. Res., 106(B6), 11 217–11 237, 2001.

~~Celis, M.R., Dennis, E.J., and Tapia, R.A.: A trust region strategy for nonlinear equality constrained optimization, in: Numerical Optimization, eds Boggs, P.T., Byrd, R.H., and Schnabel, R.B., SIAM, Philadelphia, PA (USA), 71–82, 1984.~~

Cheloni, D., D'Agostino, N., and Selvaggi, G.: Interseismic coupling, seismic potential, and earthquake recurrence on the southern front of the Eastern Alps (NE Italy), J Geophys Res-Sol Ea, 119, 4448–4468, doi:10.1002/2014jb010954, 2014.

Chen, W., Braitenberg, C., and Serpelloni, E.: Interference of tectonic signals in subsurface hydrologic monitoring through gravity and GPS due to mountain building, Glob. Planet. Change, 167, 148–159, doi:10.1016/j.gloplacha.2018.05.003, 2018.

Chery, J., Genti, M., and Vernant, P.: Ice cap melting and low-viscosity crustal root explain the narrow geodetic uplift of the Western Alps, Geophys. Res. Lett., 43, 3193–3200, doi:10.1002/2016GL067821, 2016.

Cianflone, G., Tolomei, C., Brunori, C., and Dominici, R.: InSAR Time Series Analysis of Natural and Anthropogenic Coastal Plain Subsidence: The Case of Sibari (Southern Italy), Rem. Sens., 7, 16004–16023. doi:10.3390/rs71215812, 2015.

Clark, P. U., Dyke, A. S., Shakun, J. D., Carlson, A. E., Clark, J., Wohlfarth, B., Mitrovica, J. X., Hostetler, S. W. & McCabe, A. M.: The Last Glacial Maximum. Science 325, 710–714, 2009.

Clark, P.U., Shakun, J.D., Baker, P.A., Bartlein, P.J., Brewer, S., Brook, E., Carlson, A.E., Cheng, H., Kaufman, D.S., Liu, Z., Marchitto, T.M., Mix, A.C., Morrill, C., Otto- Bliesner, B.L., Pahnke, K., Russell, J.M., Whitlock, C., Adkins, J.F., Blois, J.L., Clark, J., Colman, S.M., Curry, W.B., Flower, B.P., He, F., Johnson, T.C., Lynch-Stieglitz, J., Markgraf, V., McManus, J., Mitrovica, J.X., Moreno, P.I. & Williams, J.W.: Global climate evolution during the last deglaciation. Proc. Natl. Acad. Sci. 109 (19), E1134–E1142, 2012.

D'Agostino, N., Cheloni, D., Mantenuto, S., Selvaggi, G., Michelini, A., and Zuliani, D.: Strain accumulation in the southern Alps (NE Italy) and deformation at the northeastern boundary of Adria observed by CGPS measurements, Geophys. Res. Lett., 32, L19306, doi:10.1029/2005GL024266, 2005.

Danesi, S., Pondrelli, S., Salimbeni, S., Cavaliere, A., Serpelloni, E., Danecek, P., Lovati, S., and Massa, M.: Active deformation and seismicity in the Southern Alps (Italy): The Montello hill as a case study, Tectonophysics 653, 95–108, doi:10.1016/j.tecto.2015.03.028, 2015.

Daout, S., Barbot, S., Peltzer, G., Doin, M.P., Liu, Z., and Jolivet, R.: Constraining the kinematics of metropolitan Los Angeles faults with a slip-partitioning model, Geophys. Res. Lett., 43, 11192–11201, doi:10.1002/2016GL071061, 2016.

Devoti, R., Zuliani, D., Braitenberg, C., Fabris, P., and Grillo, B.: Hydrologically induced slope deformations detected by GPS and clinometric surveys in the Cansiglio Plateau, southern Alps, Earth planet. Sci. Lett., 419, 134–142. doi:10.1016/j.epsl.2015.03.023, 2015.

Doglioni, C.: The Venetian Alps thrust belt, in: Thrust Tectonics. Springer Netherlands, Dordrecht, pp. 319–324. doi:10.1007/978-94-011-3066-0_29, 1992.

Doglioni, C.: Thrust tectonics example from the venetian alps , Studi Geologici Camerti, vol. spec., 117-129, 1990.

Doin, M.-P., Lasserre, C., Peltzer, G., Cavalié, O., Doubre, C.: Corrections of stratified tropospheric delays in SAR interferometry: Validation with global atmospheric models. J. Appl. Geophys., 69, 35–50, 2009.

Efron, B. and Tibshirani, R.: Bootstrap Methods for Standard Errors, Confidence Intervals, and Other Measures of Statistical Accuracy. Statist. Sci., 1(1), 54-75. doi:10.1214/ss/1177013815, 1986.

Elliott, J.R., Biggs, J., Parsons, B., and Wright, T.J.: InSAR slip rate determination on the Altyn Tagh Fault, northern Tibet, in the presence of topographically correlated atmospheric delays, Geophys. Res. Lett. 35, doi:10.1029/2008GL033659, 2008.

Fantoni, R., Catellani, D., Merlini, S., Rogledi, S., and Venturini, S.: La registrazione degli eventi deformativi cenozoici nell'avampaese veneto-friulano, Mem Soc Geol It, 57, 301–313, 2002.

Fantoni, R. and Franciosi, R.: Tectono-sedimentary setting of the Po Plain and Adriatic foreland. Rend. Fis. Acc. Lincei 21, 197–209, doi:10.1007/s12210-010-0102-4, 2010.

Farr, T. G., Rosen, P. A., Car,o E., Crippen, R., Duren, R., Hensley, S., Kobrick, M., Paller, M., Rodriguez, E., Roth, L., Seal, D., Shaffer, S., Shimada, J., Umland, J., Werner, M., Oskin, M., Burbank, D. and Alsdorf, D.: The Shuttle Radar Topography Mission, Reviews of Geophysics, 45, RG2004, doi:10.1029/2005RG000183, 2007.

Feng, G., Ding, X., Li, Z., Mi, J., Zhang L., and Omura, M.: Calibration of an InSAR-Derived Coseimic Deformation Map Associated With the 2011 Mw-9.0 Tohoku-Oki Earthquake, IEEE Geoscience and Remote Sensing Letters, 9(2), 302-306, doi: 10.1109/LGRS.2011.2168191, 2012.

Ferretti, A., Savio, G., Barzaghi, R., Borghi, A., Musazzi, S., Novali, F., Prati, C., and Rocca, F.: Submillimeter Accuracy of InSAR Time Series: Experimental Validation, IEEE Trans. Geosci. Remote Sensing, 45, 1142–1153, doi:10.1109/TGRS.2007.894440, 2007.

Fontana, A., Mozzi, P., Bondesan, A.: Alluvial megafans in the Veneto-Friuli Plain: Evidence of aggrading and erosive phases during Late Pleistocene and Holocene. Quaternary International, 189(1), 71–90, 2008.

Fontana, A., Mozzi, P., & Marchetti, M.: Alluvial fans and megafans along the southern side of the Alps. Sedimentary Geology, 301, 150–171, 2014.

Frisch, W., Kuhlemann, J., Dunkl, I., and Brügel, A.: Palinspastic reconstruction and topographic evolution of the Eastern Alps during late Tertiary tectonic extrusion, Tectonophysics, 297, 1–15, doi: 10.1016/S0040-1951(98)00160-7, 1998.

Gabriel, A., Goldstein, R., and Zebker, H.: Mapping Small Elevation Changes Over Large Areas: Differential Radar Interferometry, Journal of Geophysical Research, 94(B7), 9183-9191, doi:10.1029/JB094iB07p09183, 1989.

Galadini, F., Meletti, C., and Vittori, E.: Major active faults in Italy: available surficial data, Netherlands Journal of Geosciences, 80(3-4), 273-296. doi:10.1017/S001677460002388X, 2001.

Galadini, F., Poli, M.E., and Zanferrari, A.: Seismogenic sources potentially responsible for earthquakes with M≥ 6 in the eastern Southern Alps (Thiene-Udine sector, NE Italy), Geophys. J. Int., 161, 739–762. doi:10.1111/j.1365-246x.2005.02571.x, 2005.

Gatto, P., Carbognin, L.: The Lagoon of Venice: Natural environmental trend and man-induced modification. Hydrological Science Bulletin, 26(4), 379– 391, 1981.

Ghulam A., Amer, R., Ripperdan, R.: A filtering approach to improve deformation accuracy using large baseline, low coherence DInSAR phase images, 2010 IEEE International Geoscience and Remote Sensing Symposium, Honolulu, HI, 3494-3497, doi: 10.1109/IGARSS.2010.5652581, 2010.

Goldstein, R. M. and Werner, c. L.: Radar Interferogram Filtering for Geophysical Applications, Geophys. Res. Lett., 25(21), 4035–4038, doi:10.1029/1998GL900033, 1998.

Grandin, R., Doin, M.-P., Bollinger, L., Pinel-Puysségur, B., Ducret, G., Jolivet, R., and Sapkota, S.N.: Long-term growth of the Himalaya inferred from interseismic InSAR measurement, Geology, 40, 1059–1062, doi:10.1130/G33154.1, 2012.

Hammond WC, Li Z, Plag HP, Kreemer C, and Blewitt G.: Integrated InSAR and GPS studies of crustal deformation in the Western Great Basin, Western United States, Int. A. of the Ph., Rem. Sens. and Spatial Information Sc., Kyoto Japan, XXXVIII(Part 8):39-43, 2010.

Herring, T. A., King, R. W., Floyd, M. A., McClusky, S. C., Introduction to GAMIT/GLOBK, Release 10.6. Retrieved from http://www-gpsg.mit.edu/~simon/gtgk/Intro_GG.pdf, 2015.

Hsu, Y-J., Simons, M., Yu, S-B., Kuo, L-C., and Chen, H-Y.: A two-dimensional dislocation model for interseismic deformation of the Taiwan mountain belt, Earth Planet. Sci. Lett., 211 (3–4), 287-294, doi:10.1016/S0012-821X(03)00203-6, 2003.

Jolivet, R., Lasserre, C., Doin, M.-P., Guillaso, S., Peltzer, G., Dailu, R., Sun, J., Shen, Z.-K., Xu, X.: Shallow creep on the Haiyuan Fault (Gansu, China) revealed by SAR Interferometry, J. Geophys. Res., 117, B06401, doi:10.1029/2011JB008732, 2012.

~~Johanson, I., and Bürgmann, R.: Creep and quakes on the northern transition zone of the San Andreas fault from GPS and InSAR data, Geophys. Res. Lett., 32, L14306, doi:10.1029/2005GL023150, 2005.~~

Jolivet, R., Lasserre, C., Doin, M.P., Peltzer, G., Avouac, J.P., Sun, J., and Dailu, R.: Spatio-temporal evolution of aseismic slip along the Haiyuan fault, China: Implications for fault frictional properties, Earth planet. Sci. Lett., 377-378, 23–33. doi:10.1016/j.epsl.2013.07.020, 2013.

Jònsson, S., Zebker, H. A., Segall, P., Amelung, F.: Fault slip distribution of the 1999 Mw7.1 Hector Mine, California, earthquake, estimated from satellite radar and GPS measurements, Bull. Seismol. Soc. Am., 92(4), 1377–1389, doi:10.1785/0120000922, 2002.

Lohman, R., and Simons, M.: Some thoughts on the use of InSAR data to constrain models of surface deformation: Noise structure and data downsampling, Geochem. Geophys. Geosyst., 6, doi:10.1029/2004GC000841, 2005.

Maurer, J., Johnson, K.: Fault coupling and potential for earthquakes on the creeping section of the central San Andreas Fault, J. Geophys. Res. Solid Earth, 119, doi:10.1002/2013JB010741, 2014.

Mey, J., Scherler, D., Wickert, A.D., Egholm, D.L., Tesauro, M., Schildgen, T.F., and Strecker, M.R.: Glacial isostatic uplift of the European Alps, Nature Communications, 7, 13382, doi:10.1038/ncomms13382, 2016.

Molinari, I., Verbeke, J., Boschi, L., Kissling, E., and Morelli, A.: Italian and Alpine three-dimensional crustal structure imaged by ambient-noise surface-wave dispersion, Geochem. Geophys. Geosyst. 16(12), 4405–4421. doi:10.1002/2015GC006176, 2015.

Monegato, G., Scardia, G., Hajdas, I., Rizzini, F. & Piccin, A.: The Alpine LGM in the boreal ice-sheets game. Sci. Rep. 7, 2078, 2017.

Moulin, A. and Benedetti, L.: Fragmentation of the Adriatic Promontory: New Chronological Constraints From Neogene Shortening Rates Across the Southern Alps (NE Italy), Tectonics, 105, 739–21, doi:10.1029/2018TC004958, 2018.

Mozzi, P.: Alluvial plain formation during the Late Quaternary between the southern Alpine margin and the Lagoon of Venice (northern Italy). Geografia Fisica e Dinamica Quaternaria (Suppl. 7), 219–230, 2005.

Nocquet, J.M., Sue, C., Walpersdorf, A., Tran, T., Lenôtre, N., Vernant, P., Cushing, M., Jouanne, F., Masson, F., Baize, S., Chery, J., and van der Beek, P.A.: Present-day uplift of the western Alps, Sci. Rep., 1–6, doi:10.1038/srep28404, 2016.

Norton, K.P., Hampel, A.: Postglacial rebound promotes glacial re-advances – a case study from the European Alps. Terra Nova 22 (4), 297–302, 2010.

Okada, Y.: Surface deformation due to shear and tensile faults in a half-space, Bulletin of the seismological society of America, 75, 1135-1154, 1985.

Pedersen, R., Jònsson, S., Àrnadòttir, T., Sigmundsson, F. Feigl, K.L: Fault slip distribution of two June 2000 Mw6.5 earthquakes in South Iceland estimated from joint inversion of InSAR and GPS measurements, Earth. planet. Sci. Lett., 213(3–4), 487–502. doi:10.1016/S0012-821X(03)00302-9, 2003.

Pellegrini, G.B., and Zanferrari, A.: Inquadramento strutturale ed evoluzione neotettonica dell'area compresa nei fogli 23-Belluno, 22-Feltre (p.p.) e 24-Maniago (p.p.). C.N.R. Prog. Final. "Geodinamica": contributi alla realizzazione della carta neotettonica d'Italia, Pubbl. 356, pp. 459-496, 1980.

Pellegrini, G.B., and Zambrano, R.: Il corso del Piave a Ponte nelle Alpi nel Quaternario, Studi Trentini di Scienze Naturali, LVI, 69-100, 1979.

Pellegrini, G.B., Albanese, D., Bertoldi, R. and Surian, N.: La deglaciazione alpina nel Vallone Bellunese, Alpi meridionali orientali. Geografia Fisica e Dinamica Quaternaria. Supplemento 7, 271–280, 2005.

Peltier, W.R.: Global glacial isostasy and the surface of the ice-age Earth: the ICE-5G (VM2) model and GRACE, Annu. Rev. Earth Planet. Sci., 32, 111–149. doi:10.1146/annurev.earth.32.082503.144359, 2004.

Poli, M.E., Burrato, P., Galadini, F., and Zanferrari, A.: Seismogenic sources responsible for destructive earthquakes in NE Italy, Boll. Geof. Teor. Appl., 49, 301-313, http://www3.ogs.trieste.it/bgta/pdf/bgta49.3.4_POLI.pdf , 2008.

Pondrelli, S., Ekstrom, G., and Morelli, A.: Seismotectonic re-evaluation ofthe 1976 Friuli, Italy, seismic sequence. J. Seismol., 5, 73–83, doi:10.1023/A:1009822018837, 2001.

Priolo, E., Romanelli, M., Plasencia Linares, M.P., Garbin, M., Peruzza, L., Romano, M.A., Marotta, P., Bernardi, P., Moratto, L., Zuliani, D., and Fabris, P.: Seismic Monitoring of an Underground Natural Gas Storage Facility: The Collalto Seismic Network, Seismological Research Letters, 86, 109–123, doi:10.1785/0220140087, 2015.

Ratschbacher, L., Merle, O., Davy, P., and Cobbold, P.: Lateral extrusion in the eastern Alps, Part 1: Boundary conditions and experiments scaled for gravity, Tectonics, 10, 245–256, doi:10.1029/90TC02622, 1991a.

Ratschbacher, L., Frisch, W., Linzer, H.G., Merle, O.: Lateral extrusion in the Eastern Alps, part 2: structural analysis, Tectonics, 10, 257–271, doi: 10.1029/90TC02623, 1991b.

Robl, J., Heberer, B., Prasicek, G., Neubauer, F., and Hergarten, S.: The topography of a continental indenter: The interplay between crustal deformation, erosion, and base level changes in the eastern Southern Alps. J. Geophys. Res. Earth Surf., 122, 310–334, doi:10.1002/2016JF003884, 2017.

Romano, M.A., Peruzza, L., Garbin, M., Priolo, E., and Picotti, V.: Microseismic Portrait of the Montello Thrust (Southeastern Alps, Italy) from a Dense High-Quality Seismic Network, Seismol. Res. Lett., 1–16. doi:10.1785/0220180387, 2019.

Rovida A., Locati M., Camassi R., Lolli B., and Gasperini P.: Catalogo Parametrico dei Terremoti Italiani (CPTI15). Istituto Nazionale di Geofisica e Vulcanologia (INGV), https://doi.org/10.6092/INGV.IT-CPTI15, 2016.

Schmid, S.M., F Genschuh, B., Kissling, E., Schuster, R.: Tectonic map and overall architecture of the Alpine orogen. Eclogae Geol. Helv. 97, 93–117. http://dx.doi.org/10.1007/s00015-004-1113-x, 2004.

Segall, P., Davis, J. L.: GPS applications for geodynamics and earthquake studies, Annu. Rev. Earth Planet. Sci., 23, 201–336, 1997.

Serpelloni, E., Casula, G., Galvani, A., Anzidei, M., and Baldi, P.: Data analysis of permanent GPS networks in Italy and surrounding regions: application of a distributed processing approach, Ann Geophys-Italy 49, 897–928, 2006.

Serpelloni, E., Faccenna, C., Spada, G., Dong, D., and Williams, S.D.P.: Vertical GPS ground motion rates in the Euro-Mediterranean region: New evidence of velocity gradients at different spatial scales along the Nubia-Eurasia plate boundary, J Geophys Res-Sol Ea 118, 6003–6024. doi:10.1002/2013JB010102, 2013.

Serpelloni, E., Vannucci, G., Anderlini, L., and Bennett, R.A.: Kinematics, seismotectonics and seismic potential of the eastern sector of the European Alps from GPS and seismic deformation data, Tectonophysics, 688, 157–181, doi:10.1016/j.tecto.2016.09.026., 2016.

Serpelloni, E., Pintori, F., Gualandi, A., Scoccimarro, E., Cavaliere, A., Anderlini, L., Belardinelli, M.E., and Todesco, M.: Hydrologically-induced karst deformation: insights from GPS measurements in the Adria-Eurasia plate boundary zone. J Geophys Res-Sol Ea 85, 457. doi:10.1002/2017jb015252., 2018.

Shirzaei, R., and Bürgmann, R.: Topography correlated atmospheric delay correction in radar interferometry using wavelet transfoms, Geophys. Res. Lett., 39, L01305, doi:10.1029/2011GL049971, 2012.

Slejko, D., Neri, G., Orozova, I., Renner, G., and Wyss, M.: Stress field in Friuli (NE Italy) from fault plane solutions of activity following the 1976 main shock. Bulletin of the Seismological Society of America; 89 (4), 1037–1052, 1999.

Spada, G., Antonioli, A., Boschi, L., et al.: Modeling Earth's post-glacial rebound, Eos Trans. AGU, 85(6), 62–64, doi:10.1029/2004EO060007, 2004.

Spada, G., Stocchi, P., and Colleoni, F.: Glacio–isostatic Adjustment in the Po Plain and in the Northern Adriatic Region, Pure appl. Geophys, 166, 1303–1318, doi:10.1007/s00024-004-0498-9, 2009.

Spada, G., Barletta, V.R., Klemann, V., Riva, R.E.M., Martinec, Z., Gasperini, P., Lund, B., Wolf, D., Vermeersen, L.L.A., and King, M.A.: A benchmark study for glacial isostatic adjustment codes, Geophysical Journal International, 185, 106–132, doi:10.1111/j.1365-246X.2011.04952.x, 2011.

Sternai, P., Herman, F., Champagnac, J.-D., Fox, M., Salcher, B., Willett, S.D.: Preglacial topography of the European Alps. Geology 40 (12), 1067–1070, 2012.

Sternai P., Sue, C., Husson, L., Serpelloni, E., Becker, T.W., Willett, S.D., Faccenna, C., Di Giulio, A., Spada, G., Jolivet, L., Valla, P., Petit, C., Nocquet, J.-M., Walpersdorf, A., and Castelltort, S.: Present-day uplift of the European Alps: Evaluating mechanisms and models of their relative contributions, Earth-Science Reviews, 190, 589–604, doi:10.1016/j.earscirev.2019.01.005, 2019.

Teatini, P., Tosi, L., Strozzi, T., Carbognin, L., Wegmüller, U., and Rizzetto, F.: Mapping regional land displacements in the Venice coastland by an integrated monitoring system, Rem Sens Env, 98, 403-413, doi:10.1016/j.rse.2005.08.002, 2005.

Tosi, L., Carbognin, L., Teatini, P., Strozzi, T., Wegmüller, U.: Evidence of the present relative land stability of Venice, Italy, from land, sea, and space observations, Geophys. Res. Lett., 29(12), 1562, doi:10.1029/2001GL013211, 2002.

Tsai, M-C., Yu, S-B., Hsu, Y-J., Chen, H-Y., and Chen, H-W.: Interseismic crustal deformation of frontal thrust fault system in the Chiayi–Tainan area, Taiwan, Tectonophysics, 554–557, 169-184, doi:10.1016/j.tecto.2012.05.014, 2012.

Vergne, J., Cattin, R., and Avouac, J.P.: On the use of dislocations to model interseismic strain and stress build-up at intracontinental thrust faults, Geophysical Journal International, 147, 155–162, 2001.

Waltz, R. A. , J. L. Morales, J. Nocedal, and D. Orban, "An interior algorithm for nonlinear optimization that combines line search and trust region steps," Mathematical Programming, Vol 107, No. 3, pp. 391–408, 2006.

Wang, H., and Wright, T.J.: Satellite geodetic imaging reveals internal deformation of western Tibet, Geophys. Res. Lett., 39, L07303, doi:10.1029/2012GL051222, 2012.

Wells, D.L., and Coppersmith, K.J.: New empirical relationships among magnitude, rupture length, rupture width, rupture area, and surface displacement, Bulletin of the Seismological Society of America, 84, 974–1002, 1994.

Wessel, P., and Smith, W.H.F.: New, improved version of Generic Mapping Tools released, EOS Trans. AGU, 79(47), p. 579, doi:10.1029/98EO00426, 1998.

Zanferrari, A., Pianetti, F., Mattana, U, Dell'Arche, and Toniello, V.: Evoluzione neotettonica e schema strutturale dell'area compresa nei Fogli 38 - Conegliano, 37 - Bassano del Grappa (p.p.) e 39 - Pordenone (p.p.). In CNR (1980)- Contributi alla realizzazione della Carta Neotettonica d'Italia. P.F. Geodinamica, Pubbl. 356(1), 397-435, 1980.

Zebker, H.A., Rosen, P.A., Goldstein, R.M., Gabriel, A., and Werner, C.L.: On the derivation of coseismic displacement fields using differential radar interferometry: the Landers earthquake, J. Geophys. Res., 99 (B10), 19617-19634, http://dx.doi.org/10.1029/94JB01179, 1994.

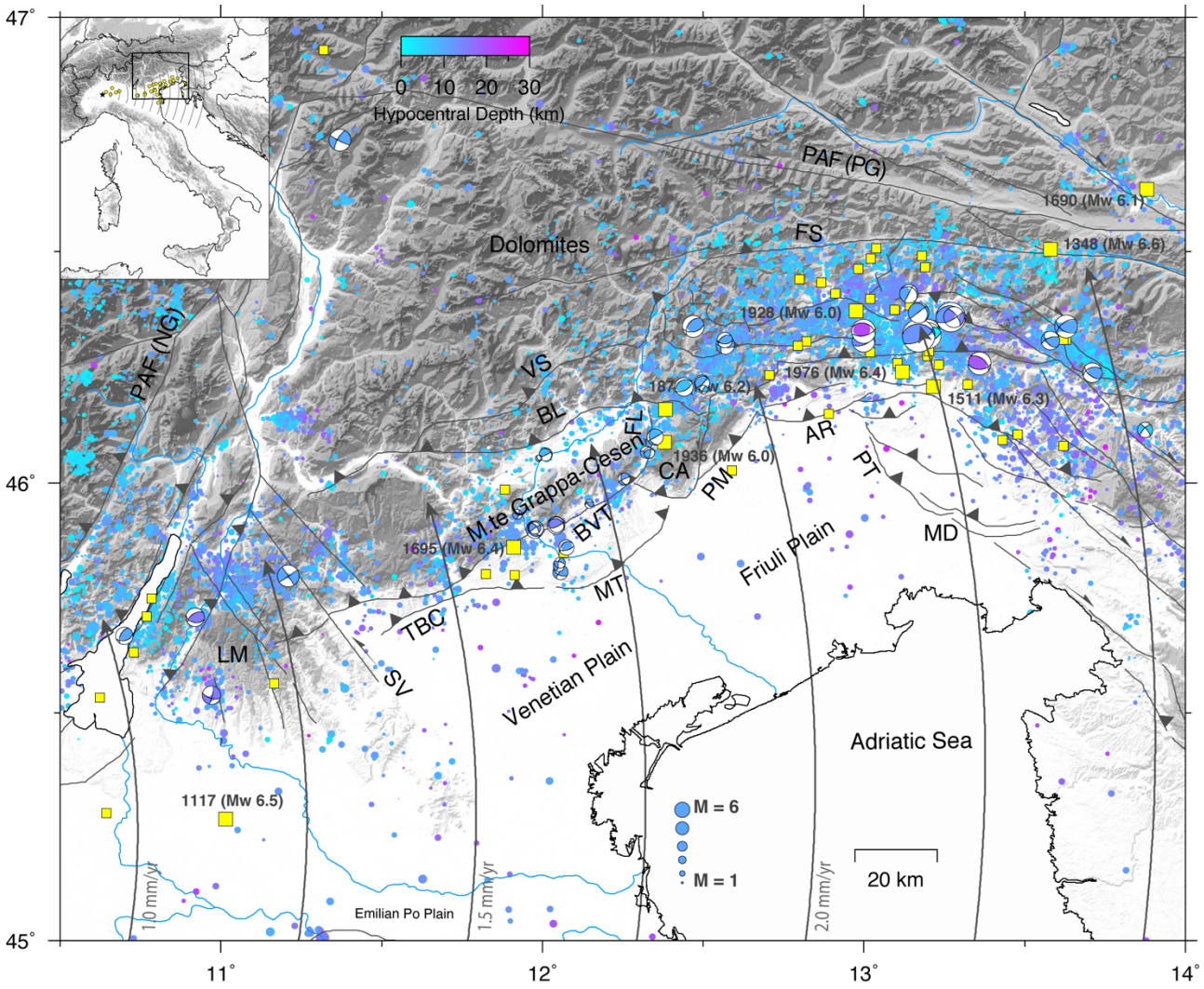

805 **Figure 1: Seismotectonic map of the study area, with the major tectonic lineaments shown in black (from Serpelloni et al., 2016). LM: Lessini Mountains; SV: Schio-Vicenza line; TBC: Thiene-Bassano-Cornuda thrust; MT: Montello thrust; BVT: Bassano-Valdobbiadene thrust; BL: Belluno thrust; VS: Valsugana thrust; CA: Cansiglio plateau; PM: Polcenigo-Maniago thrust; AR: Araba-Ragona thrust; PT: Pozzuolo thrust; MD: Medea thrust, FS: Fella-Sava line; PAF (PG): Periadriatic fault - Pusteri-Gailtal line.** ~~**The Mt Grappa- Mt Cesen anticline and the Belluno valley are indicated. Major historical events (Mw>6) are shown as light**~~
810 ~~**green squares, whereas all the historical events reported in the CPTI catalog (Rovida et al., 2016) are indicated with small dark green squares.**~~ **Major historical events (Mw>5 small squares and Mw>6 greater squares) from the CPTI catalog (Rovida et al., 2016) are shown as yellow squares. The blue-purple symbols show instrumental seismicity for the 2000-2017 time span extracted from the OGS bulletins (http://www.crs.inogs.it/bollettino/RSFVG).** ~~**The yellow-red circles show instrumental seismicity for the 2012-2018 time span recorded by the OGS Collalto seismic network (http://rete-collalto.crs.inogs.it).**~~ **The focal mechanisms (from**
815 **Anselmi et al. 2011; Danesi et al., 2015; Serpelloni et al., 2016) are plotted with the same color palette of the OGS instrumental seismicity. The small circles around the geodetic pole of rotation showing the motion direction of Adria relative to Eurasia (Serpelloni et al., 2016).** ~~**Dashed box: Location of the studied region encompassing the Montello, Bassano-Valdobbiadene and Belluno thrust faults (dashed box).**~~ **Insert map: Location of the Euler rotation pole (star), GNSS stations (yellow dots) used to define the Adria rotation pole in Serpelloni et al. (2016) and small circles of the Adria-Eurasia rotation pole with respect to the**
820 **region of interest (black box).**

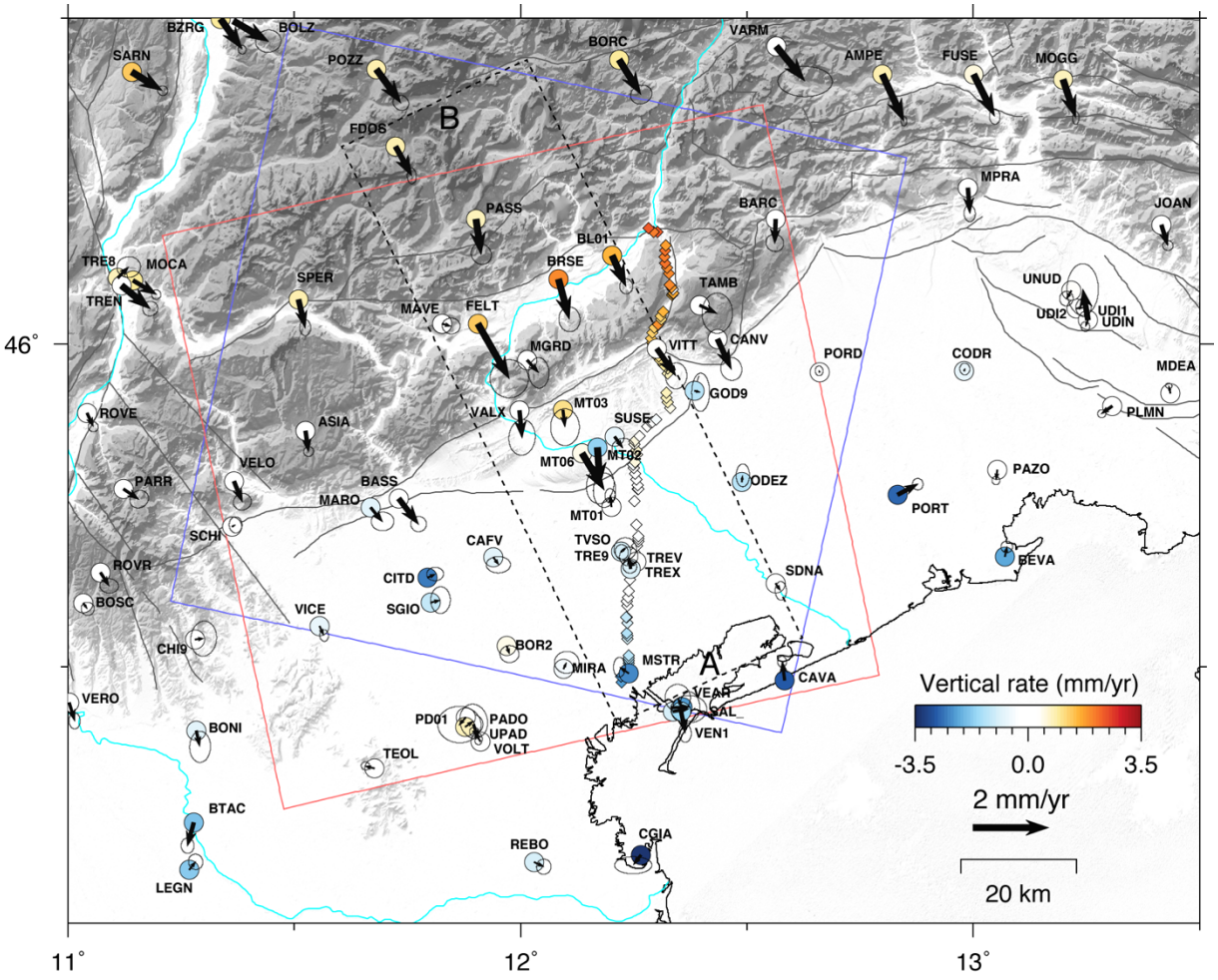

Figure 2: Geodetic dataset: the black arrows show the horizontal GPS velocities (with 95% error ellipses) in a fixed-Adria reference frame, whereas the colored circles show the vertical GPS velocities, where blue colors indicate negative (subsidence) values and red colors indicate positive (uplift) values. The colored diamonds show the vertical ground motion rates estimated from the IGM leveling data in the 1952-1984 time interval, using the same color scales of the GPS velocities. The blue and red squares indicate the ascending and descending ENVISAT frames, respectively, used in this work. The dashed box shows the A-B cross section shown in Fig. 3.

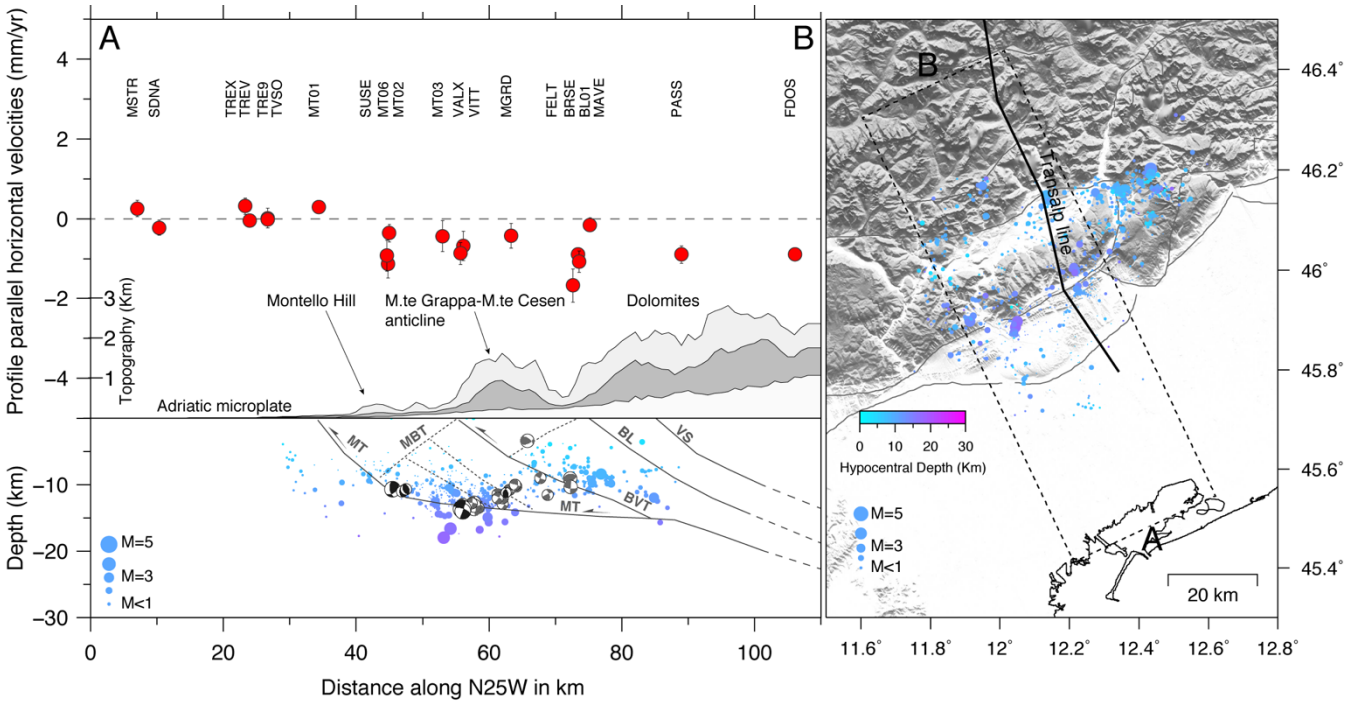

Figure 3: [left panel] Cross section of GPS velocities, topography, instrumental seismicity and focal mechanisms included in the dashed box of Fig. 2 (and the right panel). Profile-parallel velocity components, in a fixed-Adria reference frame (see Fig. 2), are shown as red circles, with 1σ error bars in gray. The dark gray areas show the average (median) topography in the profile swath, with the light gray and white areas showing the maximum and minimum elevations, respectively. The blue-purple circles show instrumental seismicity, in the 2012-2017 time interval, relocated from Romano et al. (2019), as function of depth and scaled with magnitude. The gray and black focal mechanisms are from Anselmi et al. (2011) and Danesi et al. (2015), respectively. The gray continuous and dashed lines represent major and secondary faults digitized from the TRANSALP profile interpretation (modified from Fig. 11 of Castellarin et al., 2006). MT = Montello thrust, MBT = Montello backthrust, BV = Bassano–Valdobbiadene thrust, BL = Belluno thrust, VS = Valsugana thrust. [right panel] Map showing the instrumental seismicity recorded by the Collalto seismic network (Priolo et al., 2015) relocated by Romano et al. (2019), the swath profile (dashed box) and the TRANSALP line (black line). ~~Cross section showing observed horizontal velocities, in a fixed-Adria reference frame (see Fig. 2), across the A–B profile in Fig. 2. Profile-parallel velocity components for GPS stations included in the dashed box of Fig. 2 are shown as red circles, with 1σ error bars in gray. The dark gray areas show the average (median) topography in the profile swath, with the light gray and white areas showing the maximum and minimum elevations, respectively. The distribution of seismicity with depth (in km), inside the dashed box of Fig. 2 is shown by the colored circles, where, as in Fig. 1, the blue-purple circles show instrumental seismicity for the 2000-2017 time span extracted from the OGS bulletins (http://www.ers.inogs.it/bollettino/RSFVG) and the yellow-red circles show instrumental seismicity for the 2012-2018 time span recorded by the OGS Collalto seismic network (http://rete-collalto.ers.inogs.it), and relocated by Romano et al. (2019). The gray and black focal mechanisms are from Anselmi et al. (2011) and Danesi et al. (2015), respectively. The gray continuous and dashed lines represent major and secondary faults digitized from the TRANSALP profile interpretation (modified from Castellarin et al., 2006). MT = Montello thrust, MBT = Montello backthrust, BV = Bassano–Valdobbiadene thrust, BL = Belluno thrust, VS = Valsugana thrust.~~

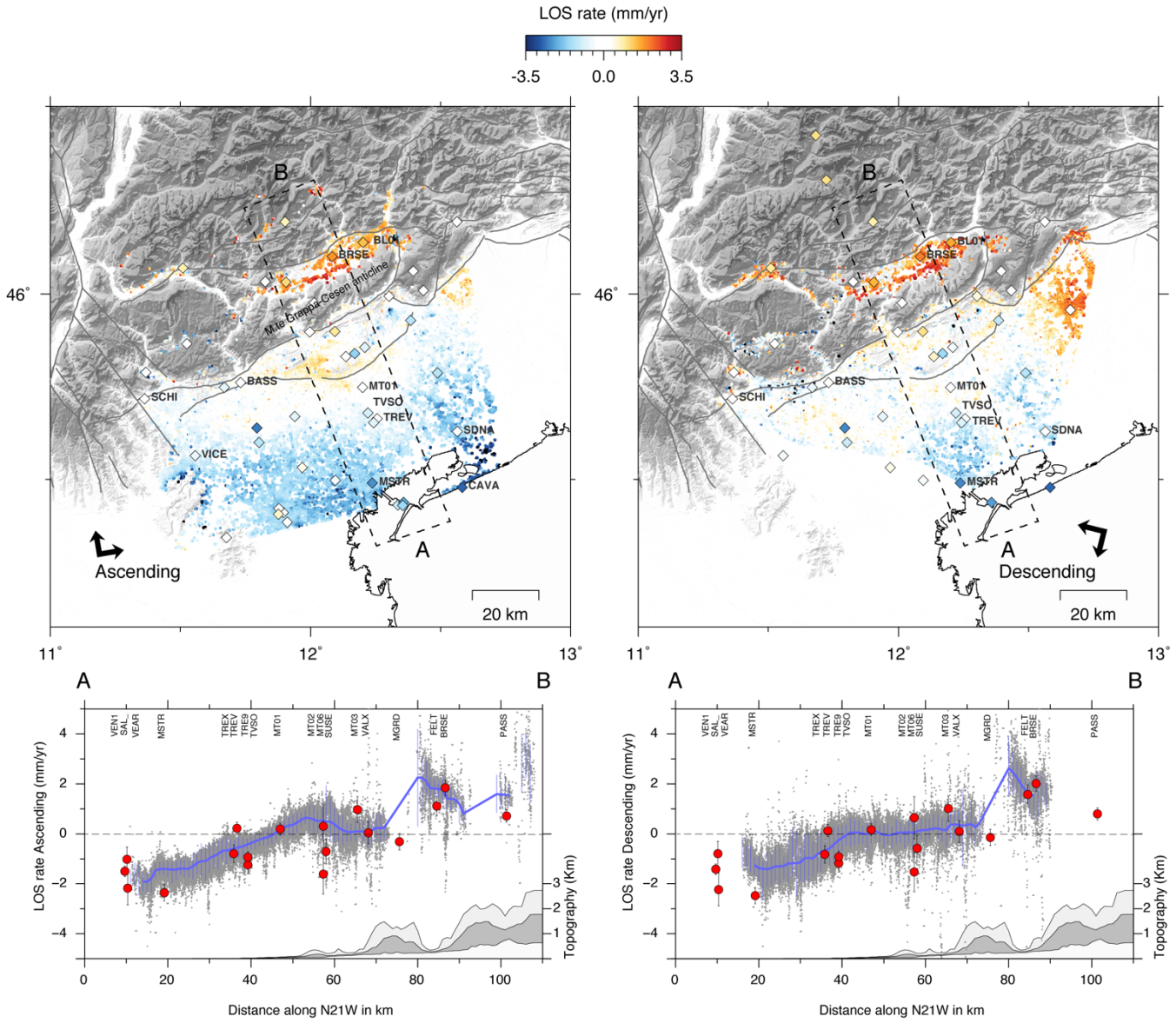

Figure 4: InSAR line-of-sight (LoS) velocities (after the ramp removal, see Section 3.3 of the main text for details) for the ascending (left) and descending (right) orbits, with negative (blue) and positive (red) values indicating increasing and decreasing distance between the Earth surface and the satellite. Colored diamonds indicate the 3D GPS velocities projected along the SAR LoS directions. Bottom panels show the SAR and GPS LoS velocities (red circles with 1σ error bars in gray) along the A-B cross section (dashed box) for the ascending and descending orbits, respectively. The blue line indicates the median value of the InSAR data along cross section, given the minimum number of 50 SAR pixels in each bin of 1 km, and the light bars represent the data dispersion for each bin.

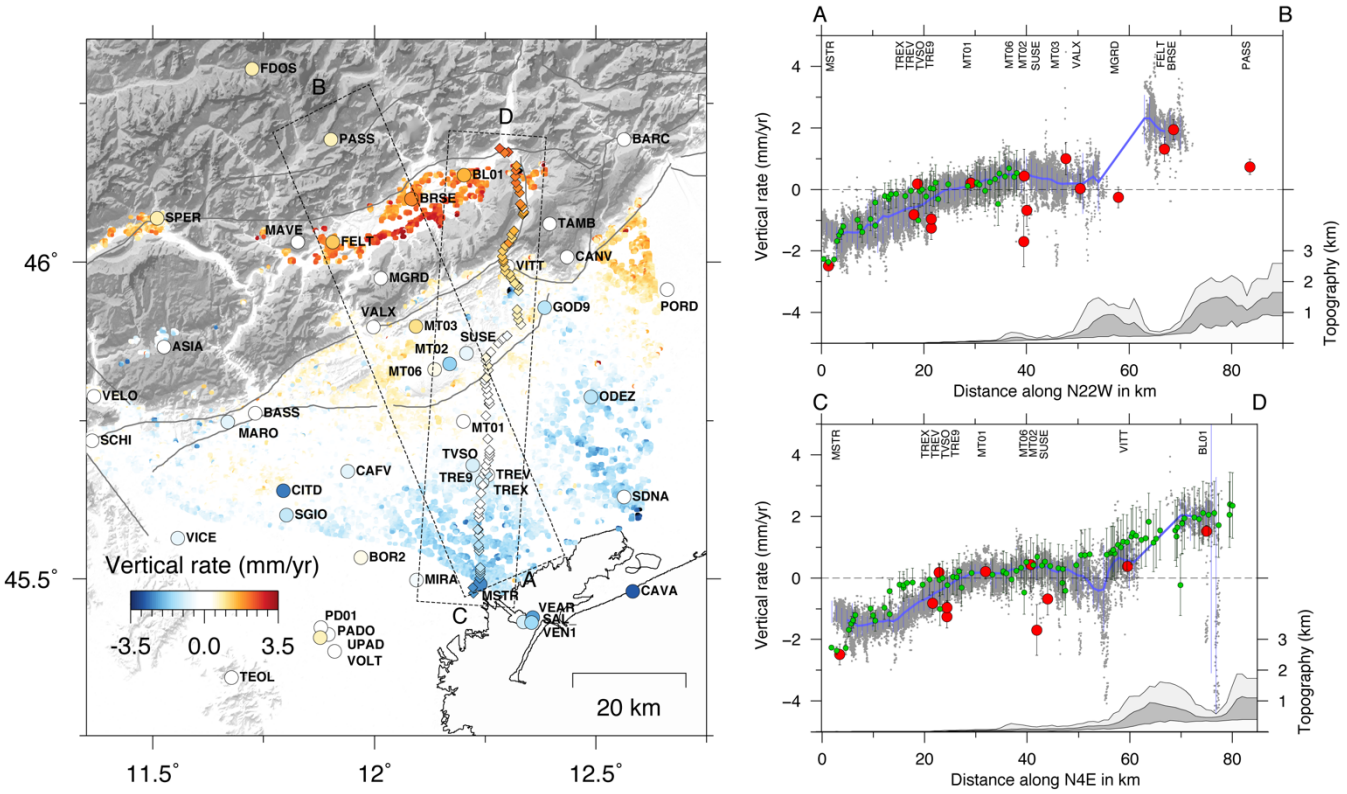

Figure 5: Left: Vertical velocity field from InSAR data decomposition (dots), from GPS measurements (circles) and from the IGMI leveling data (diamonds), where blue colors indicate negative (subsidence) values and red colors indicate positive (uplift) values. Right: cross sections of vertical velocities along the A-B (top) and the C-D profile (bottom). The blue lines and red circles are the same as in Fig. 4.

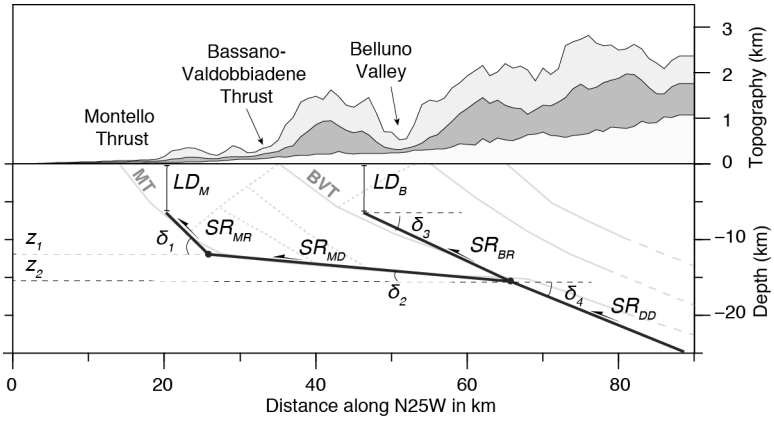

Figure 6: Sketch of the geometries for two-dimensional fault model as described in Section 4. LDM (locking depth of Montello fault), LDB (locking depth of Bassano fault), SRMR (slip rate of Montello Ramp), SRMD (slip rate of Montello Decollement), SRBR (slip rate of Bassano Ramp) and SRDD (slip rate of the Deep Ramp) are the fault parameters estimated from the data inversion (see Table 2). The dip angles of each fault segment (δ1 = 45°, δ2 = 5°, δ3 = 25°, δ4 = 22°) and the depth of fault junctions (z1 = 12 km, z2 = 15.5 km) have been keep fixed.

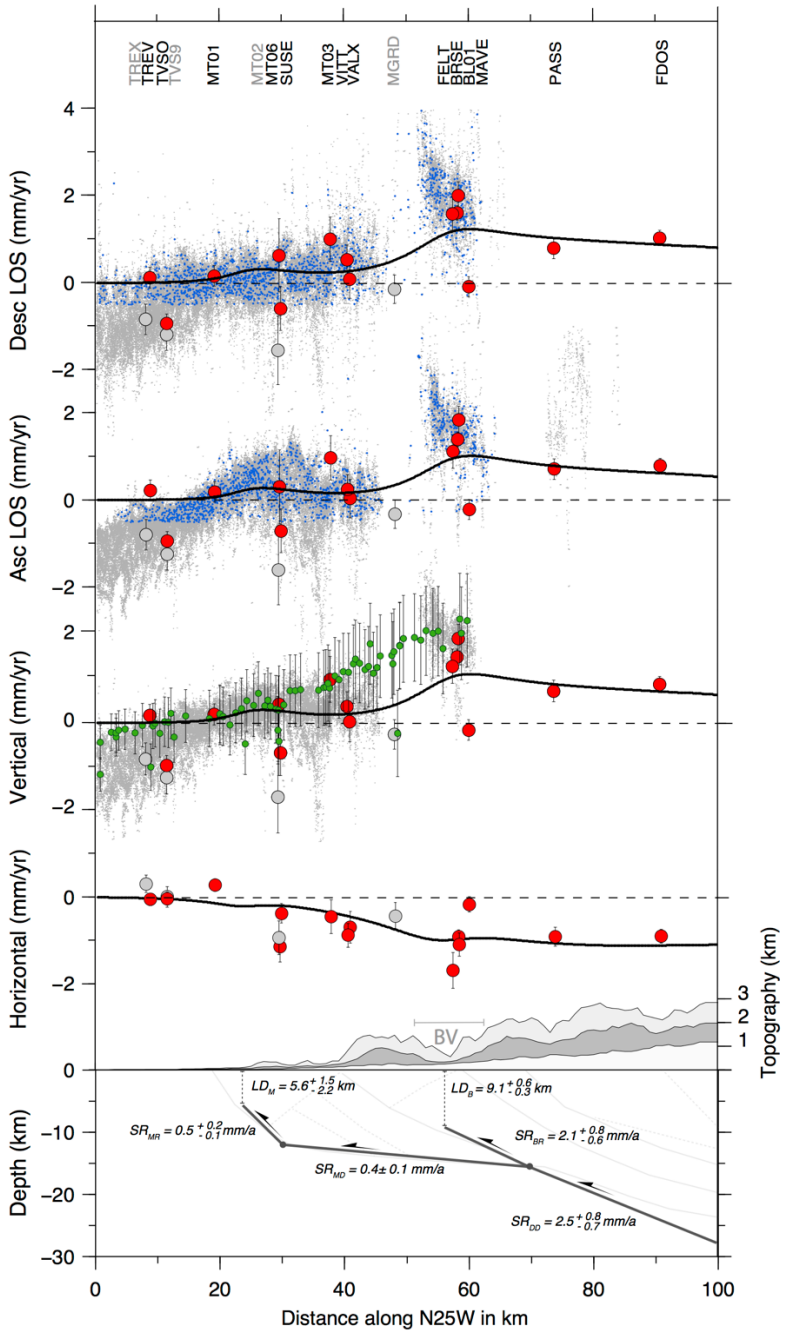

Figure 7: Cross sections, across the A-B profile in Fig. 2, showing the modeled (black lines) horizontal and vertical velocities, as well as the SAR ascending and descending LoS rates, along with the measured ones. Gray-colored GPS sites have not been used in the inversion, unlike the red ones. G~~g~~reen points indicate leveling data and small blue dots represent the subsampled InSAR LOS rates used during the inversion, displayed along with the un-subsampled InSAR dataset (light gray points). The bottom panel reports the optimal fault geometry with dip-slip rates and locking depths estimates and 95 percentile confidence bounds ~~1σ error bounds~~ (see Section 5 for details). BV: Belluno valley.